Department of Mathematics and Statistics

Mathematical Modelling of Particle-fluid Flows in Microchannels

Kittisak Chayantrakom

This thesis is presented for the Degree of

Doctor of Philosophy of

Curtin University of Technology

January 2009

Declaration

To the best of my knowledge and belief this thesis contains no material previously published by any other person except where due acknowledgment has been made.

This thesis contains no material which has been accepted for the award of any other degree or diploma in any university.

Kittisak Chayantrakom

21 January, 2009

Acknowledgments

I would like to express my gratitude to my supervisor, Professor Yong Hong Wu, for his valuable guidance . His helpful suggestions and encouragement have been of great value to me in the research and the preparation of this thesis. I would also be grateful to my associate supervisor, Associate Professor Benchawan Wiwatanapataphee, for her helpful advices and suggestions.

I would like to thank Royal Thai Government for the financial support during the period of my study. I would also like to thank Mahidol University for providing me the opportunity to study in Perth. I deeply appreciate the Office of Education Affairs, Royal Thai Embassy in Canberra for all their kind assistance during my study.

Finally, I am so thankful to the Department of Mathematics and Statistics, Curtin University of Technology for providing me with all the necessary facilities for my research. I also appreciate all the staff and students in the Department of Mathematics and Statistics for their friendship and encouragement during my study at the University.

Abstract

Flows of fluids and solid particles through microchannels have a very wide range of applications in biological and medical science and engineering. Understanding the mechanism of microflows will help to improve the development of the devices and systems in those applications. The aim of this study is to develop a sophisticated simulation and analysis technique for the study of fluid-particle flow through microchannels. This work involves construction of mathematical models, development of analytical methods and numerical algorithms, and numerical investigation and analysis.

The study consists of three parts. The first part of the research focuses on the transient flow of an incompressible Newtonian fluid through a micro-annual with a slip boundary. The flow of the fluid is governed by the continuity equation and the Navier-Stokes equations, and is driven by the pressure field with a time-varying pressure gradient. By using the Fourier series expansion in time and Bessel functions in space, an exact solution is derived for the velocity field. The velocity solution is then used to obtain the exact solutions for the flow rate and the stress field. Based on the exact solutions, the influence of the slip parameter on the flow behaviour is then investigated.

The second part of the research focuses on the particle-fluid flow in microchannels. The transport of fluid in the vessel is governed by the continuity equation and the transient Navier-Stokes equations, while the motion of the particles is governed by Newton's laws. The particle-wall and particle-particle interactions are modelled by the interacting forces, while the particle-fluid interaction is described

by the fluid drag force. A numerical scheme based on the finite element method and the Arbitary Lagrangian-Eulerian method is developed to simulate the motion of the particles and the fluid flow in the vessels. The influence of boundary slip on the velocity field in the fluid is also investigated numerically.

Based on the work in the second part, the third part of the research focuses on the control of the movement of particles in the fluid by applying an external magnetic field to the system. Maxwell's equations are used to model the magnetic field generated by the external magnetic source, and a finite element based numerical scheme is developed to solve the underlying boundary value problem for the magnetic flux density generated. From the computed flux density and magnetic vector potential, the magnetic forces acting on the particles are determined. These magnetic forces together with the drag force and the particle-particle interacting forces dominate the behaviour of the particle motion. A numerical scheme, similar to that for the second part of the research, is then developed to study the fluid-particle flow in microchannels under magnetic forces, followed by a numerical investigation on the influence of the magnetic forces on the particle flow behaviour.

List of Publications Related to This Thesis

1. B. Wiwatanapataphee, K. Chayantrakom, and Y.H. Wu, Mathematical Modelling and Numerical Simulation of Fluid-Magnetic Particle Flow in a Small Vessel, *International Journal of Mathematical Models and Methods in Applied Sciences*, 2008, 209–215.

2. B. Wiwatanapataphee, Y.H. Wu, M. Hu and K. Chayantrakom, Study of Transient Flows of Newtonian Fluids Through Micro-annuals with Slip Boundary, *Journal of Physics A: Mathematical and Theoretical*, 42(6), 2009, 065206–065219.

Contents

List of Figures

List of Tables

Nomenclature

$\mathbf{A}$	magnetic vector potential
$\mathbf{B}$	magnetic flux density
$\mathbf{F}_q$	collision force of the qth particle
$\mathbf{F}_{q,p}$	particle-particle interaction force
$\mathbf{F}_{q,w}$	particle-wall interaction force
$\mathbf{F}_{\mathrm{mag}}$	magnetic force acting on the particles
$\mathbf{F}_v$	fluid drag force acting on the particles
$\mathbf{H}$	magnetic field strength
$\mathbf{J}$	Jacobian matrix
J_0, J_1	zero-order and first order Bessel functions of the first kind
L_{enter}	entrance length of the fictitious inlet for laminar flow
$\mathbf{M}$	magnetization of the magnetic particles
Q	flow rate of fluid flux
R	outer radius of annulus
R_q	radius of the qth particle
$\mathbf{V}_q$	velocity vector of the qth particle
$\mathbf{X}$	coordinates of the reference system
$\mathbf{X}_q$	center of the qth particle
Y_0, Y_1	zero-order and first order Bessel function of the second kind
$\mathbf{d}$	rate of deformation tensor
$d_{q,p}$	distance between the centers of the qth and the pth particle
$d_{q,w}$	distance between the centers of the qth particle and the imaginary particle on the other side of the wall
l	normalized slip parameter
l_1	slip parameter of the surface of the inner annulus
l_2	slip parameter of the surface of the outer annulus

m_q	mass of the qth particle
p	pressure of fluid
p_{enter}	entrance pressure at the channel inlet
t	time
u	velocity vector of fluid in annulus
u_i	velocity component of fluid in the ith-direction
u_{mean}	average velocity of the laminar flow
v_{st}	velocity component of the solid surface on the tangential direction
v_t	velocity component of the fluid on the tangential direction
$\mathbf{x}$	coordinates of the moving coordinate system
ε_q	stiffness parameter of the qth particle
ε_w	stiffness parameter of the wall
Ω	spatially fixed domain
Ω_{def}	deformed domain
Ω_q	domain of the qth particle
$\mathbf{\Psi}$	mesh velocity
μ, μ_f	viscosity of fluid
μ_r	relative permeability of a magnetic material
μ_0	permeability in vacuum
ρ, ρ_f	density of fluid
σ_{ij}	stress-deformation rate

Chapter 1

Introduction

1.1 Background

Recent advance in microtechnologies has led to the development of many biological and engineering devices and systems in microscales. Typical examples include biochemical lab-on-the-chip systems, micro-electromechanical systems (MEMS), fuel cell devices, biological sensing and energy conversion devices [58], and drug delivery systems [76]. Most of these devices and systems involve flows of fluids and particles in microchannels, referred to as microflows [10, 33, 35, 37]. Since the functional characteristics and physical phenomena of the systems are determined by the behaviour of fluid and particle flow in these systems, it is extremely important to study the mechanism of microflows in order to gain better understanding [5, 28, 85].

In recent years, many research projects involving fluid or particle flow study have been undertaken. In the lab-on-the-chip application, it has been reported that the DEParray(tm) Chip can be used to capture and control movement of lipid microparticles [80]. Microfluidic devices integrated with a DNA computer model can be used for medical diagnostics and drug screening [49]. Nanocrystalline diamond with Chromatin immunoprecipitation protocols (ChIP)can be used for analyzing DNA [43]. Magnetic beads are separated from fluid in microfluidic channels using microelectromagnets [72]. For the MEMS application, the microthermal preconcentrators (μTPCs) is used for gas analysis of volatile organic compounds (VOCs) [2]. A MEMS viscometer is used in the oil well logging process by an-

alyzing the density and viscosity of fluids [26]. A microfluidic device consisting of MEMS-fabricated channels is used to produce microbubbles [69]. A micro-rheometer is used as a tool to measure the linear viscoelastic properties of small volumes of a fluid [19]. For the fuel cell application, a polymeric electrolyte membrane (PEM) is used to produce fuel cell from methanol gas by conducting the protons that are generated by the catalytic oxidation of the gas at the anode [39]. A microbial fuel cell (MFC) can be used as an electricity generator by converting bio-chemical energy to electrical energy [31].

Another important process which involves fluid-particle flow is the targeted drug delivery in cancer therapies. Cancer is one of the most threatening diseases that cause death to human beings. The growth rate of tumor depends on the angiogenesis which is the process in which new blood vessels develop from an existing vasculature through endothelial cell sprouting, proliferation and fusion [64]. Nutrient supplied via new blood vessels results in proliferating of cancer cells, which is in favor of tumor growth. Tumor cells need an adequate blood supply in order to perform vital cellular functions. The modern-day approach to cancer treatment is a multidisciplinary one involving varying combination of surgery, radiation therapy, chemotherapy and targeted therapies. In targeted therapies, a medication or drug is controlled to target a specific pathway in the growth and development of a tumor. Although most of the drugs used to date have proven to be successful on small animals such as mice [30, 86], their efficiency in humans remains highly variable from one patient to another.

Understanding the flow of blood and drug in the capillary bed is very important for investigating the efficiency of drug treatment as they pass from the parent blood vessel to tumor surface via an associated capillary bed. Over the last 15 years, a number of mathematical models for blood vessel formation [12, 47], blood flow and/or particle flow in capillary networks [75, 66, 60, 32] in the area of tumor-induced angiogenesis have been developed. One of these is magnetically targeted drug delivery, which was first introduced by Mosbach and Schroder [57]. This approach involves binding a drug to small biocompatible magnetic particles with

diameters less than $5\mu m$. On the surface, the particles are coated with a surfactant to functionalise some specific tasks. These particles are injected to the blood circulation system and are guided to tumor sites using an external magnetic field. Once targeted to the locations wanted, these particles release drugs to kill the cancer cells on the wall of blood vessel. This treatment has many advantages. Firstly, the size of nanoparticles carrying drugs is small enough to avoid being detected and eliminated from human immune system. The mechanism of magnetic guidance can extend the duration for the particles to be captured to the disease sites. Thus it can release drugs more efficiently.

Driscoll *et al.* [24] had studied magnetically targeted drug delivery by tracking each individual particle under the influence of Stokes drag force and magnetic force. Grief and Richardson [32] conducted a theoretical analysis of targeted drug delivery using magnetic particles and proposed a two-dimensional network model. In their model, the motion of fluid is described by Poiseuille flow, while the motion of a magnetic particle, due to balancing hydrodynamic and magnetic force, is governed by an advection-diffusion equation for the particle concentration. They found that drug targeting can be achieved by pulling magnetic particles to the edge of the vessel, and that the use of magnetically targeted drug delivery with an externally applied magnetic field is appropriate only for targets close to the surface of the body.

Although intensive research relating to the fluid-particle flow in microchannel and their applications in magnetically targeted drug delivery has been conducted, there are still some aspects that are not fully understood. The use of mathematical models will allow us to gain more understanding of fluid flow, particle flow in fluid, and the interaction between fluid and particles under a magnetic field.

1.2 Objectives

Based on the previous research, in this project, we will study the fluid-particles flow in microchannels under magnetic field. The specific objectives include the

following

(i) Study the transient behaviour of fluid flow through micro-annulus with boundary slip with particular emphases on the influences of boundary slip on the transient flow rate, velocity and stresses fields.

(ii) Construct a mathematical model and numerical scheme to study the particle-fluid flow in microchannels.

(iii) Construct a mathematical model and numerical scheme to determine the magnetic forces acting on particles by external magnetic sources, and then study the particle motion in fluids under magnetic forces.

1.3 Outline of the Thesis

This thesis consists of six chapters. Chapter one gives the background of the research highlighting the importance of the subject of fluid-particle flow in microchannels. Some specific applications which involve particle-fluid flow are reviewed with particular emphases on the magnetic drug targeting. The objectives are also given in this chapter.

Chapter two reviews relevant theories and previous work closely related to the scope of this study.

Chapter three studies the pressure driven transient flow of a Newtonian fluid in micro-channels. Exact solutions for the velocity and stress fields are derived and the effect of boundary slip is investigated based on the exact solutions.

Chapter four presents a mathematical model and numerical scheme for simulating particle-fluid flows utilizing the finite element method and the arbitary Lagragian-Eulerian method. The influence of boundary slip on the velocity and stress fields are also presented.

Chapter five presents the boundary value problem and numerical scheme for the determination of the magnetic vector potential and magnetic forces, followed by the modelling of particle movement in fluids under magnetic forces. A numerical

investigation on the influence of the magnetic field on the particle motion is also presented.

Chapter six presents the conclusions from this study. Further researches are also given in this chapter.

Chapter 2

Literature Review

2.1 General Overview

In this chapter, we review the basic theories and previous work relevant to the study of fluid-particle flow under magnetic forces. In section 2.2, the basic theories for the determination of magnetic fields and magnetic forces are presented. In section 2.3, a review of the fundamental theories for the flow of fluids are given followed by previous work on the development and applications of the subject. In section 2.4, the principal approaches and numerical techniques for simulating the flow of solid particles in fluid is reviewed.

2.2 Modelling of Magnetic Field

Magnetic fields are generated by a magnetic material such as, bar magnets and Earth. The magnetic fields exert forces on electric charges that enter to the field. Unlike electric fields, the magnetic fields only interacts with electric charges that are moving. In addition, the simplest magnetic objects are dipoles.

There are two types of magnetic field: the magnetic induction field $\mathbf{B}$ and the magnetic field $\mathbf{H}$. The magnetic induction field $\mathbf{B}$ (unit of T) is the actual magnetic field. By Faraday's law, the time variation of the magnetic flux $\Phi_{\mathbf{B}}$ generates the electric field. The magnetic field H is the field that is produced by a wire carrying current. Its strength $H = |\mathbf{H}|$ is proportional to the number of turns of that wire.

The magnetic dipole moment $\mathbf{m}$ of a magnetic material is defined as the

strength of the magnetic field. The magnetic field is proportional to $|\mathbf{m}|$ and inversely proportional to r^3, where r is a distance from the outer of the dipole. The magnetization $\mathbf{M}$ of a magnetic object is defined as the magnetic moment per unit volume, that is,

$$\mathbf{M} = \frac{\mathbf{m}}{V}, \tag{2.1}$$

where V is the volume of the material. This property determines the maximum magnetic by an object that is fully magnetized.

The magnetic force exerted on a dipole $\mathbf{m}$ by a non-uniform static magnetic field $\mathbf{H}$ is given by [74]

$$\mathbf{F} = \nabla(\mathbf{m} \cdot \mathbf{H}). \tag{2.2}$$

If the current producing the magnetic field does not overlap with the current distribution of the magnetic dipole, we have

$$\nabla \times \mathbf{H} = \mathbf{0}. \tag{2.3}$$

Recall a vector identity

$$\nabla(\mathbf{a} \cdot \mathbf{b}) = \mathbf{b} \times (\nabla \times \mathbf{a}) + \mathbf{a} \times (\nabla \times \mathbf{b}) + (\mathbf{b} \cdot \nabla)\mathbf{a} + (\mathbf{a} \cdot \nabla)\mathbf{b}. \tag{2.4}$$

Using (2.3) and (2.4), and assuming that the magnetic dipole is small, the magnetic force in (2.2) becomes

$$\mathbf{F} = (\mathbf{m} \cdot \nabla)\mathbf{H}. \tag{2.5}$$

In vacuum, the relation between $\mathbf{B}$ and $\mathbf{H}$ is given by

$$\mathbf{B} = \mu_0 \mathbf{H}, \tag{2.6}$$

where $\mu_0 = 4\pi \times 10^{-7}\,\mathrm{T} \cdot \mathrm{m} \cdot \mathrm{A}^{-1}$ is the permeability of free space.

Inside materials, the three vector fields $\mathbf{B}, \mathbf{H}$ and $\mathbf{M}$ are related by the constitutive relation

$$\mathbf{B} = \mu_0(\mathbf{H} + \mathbf{M}). \tag{2.7}$$

In magnetostatic problems, a generalized form of the constitutive relation for the magnetic field is given by

$$\mathbf{B} = \mu_0 \mu_r \mathbf{H} + \mathbf{B}_r, \tag{2.8}$$

where the dimensionless number μ_r is the relative magnetic permeability, and $\mathbf{B}_r$ is the remanent magnetic flux density, which is the magnetic flux density when no magnetic field is present.

Based on the above relations, materials are classified into three categories: paramagnetic, diamagnetic, and ferromagnetic.

In paramagnetic and diamagnetic objects, the magnetic field $\mathbf{B}$ is linearly proportional to $\mathbf{H}$,

$$\mathbf{B} = \mu_0 \mu_r \mathbf{H}. \tag{2.9}$$

If $\mu_r > 1$, the material is paramagnetic. If $\mu_r < 1$, the material is diamagnetic. The value μ_r usually differs from unity by a factor of 10^{-5}.

For material that are not permanent magnets, $\mathbf{M}$ and $\mathbf{H}$ are linearly related by

$$\mathbf{M} = \chi_m \mathbf{H}, \tag{2.10}$$

where χ_m is the magnetic susceptibility and is dimensionless.

Substituting (2.10) into (2.7), we obtain

$$\mathbf{B} = \mu_0 (1 + \chi_m) \mathbf{H}. \tag{2.11}$$

Comparing (2.11) and (2.9), we have

$$\mu_r = 1 + \chi_m. \tag{2.12}$$

Thus, for a paramagnetic material, $\chi_m > 0$, and for a diamagnetic material, $\chi_m < 0$.

In general, the governing equations for the electromagnetic field consist of the Maxwell's equations and the constitutive equations. The Maxwell's equations are as follows:

$$\nabla \times \mathbf{H} = \mathbf{J} + \frac{\partial \mathbf{D}}{\partial t}, \tag{2.13}$$

$$\nabla \times \mathbf{E} = -\frac{\partial \mathbf{B}}{\partial t}, \tag{2.14}$$

$$\nabla \cdot \mathbf{B} = 0, \tag{2.15}$$

$$\nabla \cdot \mathbf{D} = \rho_d, \tag{2.16}$$

where $\mathbf{H}$ is the magnetic field, $\mathbf{E}$ is the electric field, $\mathbf{J}$ is the total current density, $\mathbf{D}$ is the electric displacement, ρ_d is the free charge density, and $\mathbf{B}$ is the magnetic flux density. The constitutive equations are

$$\mathbf{B} = \mu\mathbf{H}, \tag{2.17}$$

$$\mathbf{D} = \varepsilon\mathbf{E}, \tag{2.18}$$

$$\mathbf{J_e} = \sigma(\mathbf{E} + \mathbf{v} \times \mathbf{B}) + \rho_d\mathbf{v}, \tag{2.19}$$

where σ is the electric conductivity, and v is the velocity. Since metal materials are good conductors, it can be assumed that the field that changes in one part of the system radiates to other part instantaneously. Therefore, $\frac{\partial \mathbf{D}}{\partial t}$ can be neglected and (2.13) becomes

$$\nabla \times \mathbf{H} = \mathbf{J}. \tag{2.20}$$

If the magnetic Reynolds number is very small, the term $(\mathbf{v} \times \mathbf{B})$ in (2.19) can be neglected. The Maxwell's equations together with the constitutive equations can be simplified to the following systems:

$$\nabla \times \mathbf{H} = \mathbf{J}, \tag{2.21}$$

$$\nabla \times \mathbf{E} = -\frac{\partial \mathbf{B}}{\partial t}, \tag{2.22}$$

$$\nabla \cdot \mathbf{B} = 0, \tag{2.23}$$

$$\nabla \cdot \mathbf{D} = 0, \tag{2.24}$$

$$\mathbf{B} = \mu\mathbf{H}, \tag{2.25}$$

$$\mathbf{J_e} = \sigma\mathbf{E}. \tag{2.26}$$

A number of mathematical models and numerical methods for modelling magnetic fields in fluid flows have been carried out. In 2000, Oldenburg et al. [59] studied the flow of ferrofluids in porous media caused by an external magnetic field due to the magnet. To simulate the flow, the external magnetic field, the magnetic field strength and its gradient were calculated by direct equations in two flow characteristics: miscible and immiscible flows. Then the magnetic body force was obtained using the force balance equations solved by the integral finite difference

method. Compared to the experimental results, the two ferrofluid models provide some new simulation capabilities. In 2002, Voltairas et al. [84] developed a general theory based on the ferrohydrodynamics to describe the magnetic drug targeting. They demonstrated that their analytical results, based on the Stokes model, agree with the experimental results in a carotid artery. They derived an upper bound of the mean blood velocity which depends on the external applied magnetic field.

In 2003, Li and Kwok [48] presented a lattice Boltzmann model using a single-relaxation-time approximation as a collision model for studying microfluidic problems which include external pressure and the Lorentz force from external electric and magnetic fields. This model can be potentially applied to magnetic drug targeting. The numerical results are in good agreement with the experimental results in the case of pressure-driven microchannel flows. In 2004, Loukopoudos and Tzirtzilakis [51] derived a mathematical model for biomagnetic fluid dynamics for the flow of the biofluid under an external magnetic field. The numerical results, obtained from the finite difference method, show the effects of a magnetic field on the flow of a biomagnetic fluids including vortex arising and increase in temperature, skin friction coefficient and heat transfer rate with an increase in the magnetic field strength. In 2006, Tzirtzilakis [83] et al. developed a mathematical model, based on the Reynolds averaged Navier- Stokes (RANS) equations, to simulate the turbulent flow of a biomagnetic fluid with a locally applied magnetic field. The low Reynolds number $k - \epsilon$ turbulence model was used for the turbulence formulation. The computational results show that, when compared between laminar and turbulent flow, the turbulence causes huge reduction on the effect of the magnetic field.

A lot of mathematical models and numerical methods for the motion of particles in fluid flow under an external magnetic field have been developed. In 1984, Driscoll [24] et al studied magnetic targeting of magnetic microspheres carrying drugs to tumorous microvasculature in rat tails. Their calculations of the magnetic force required to move microspheres to blood vessel walls, the fluid drag force, and the interparticle force were used for the analysis of microsphere capture from the experiment. In 2005, Rotariu and Strachan [65] investigated magnetic targeting of

drugs in tumor capillaries deep inside the human body using magnetic particles and an external needle magnet. A two dimensional finite element model based on the FEMM software using the magnetohydrodynamics and the motion of particles was used to solve the problem. The numerical results show that the particles of size 1 μm can be captured at a distance up to 15 cm.

Aviles et al. [7] presented a two dimensional Newtonian model with magnetic forces and used FEM to simulate the movement of magnetic drug carrier particles used to treat carotid artery diseases under the affect of an external magnetic field. In addition to a permanent magnet, the use of a near-skin implanted ferromagnetic wire was shown to improve the collection efficiency of the magnetic particles. Ally et al. [4] used the finite element package ANSYS to study magnetically targeted aerosols in lung cancer. They computed drag forces using the Stokes flow and the magnetic forces were used to calculate the motion of particles by Newton's second law. The experimental results and numerical results are in good agreement and show that the magnetic field gradient and aerosol particle concentration are important factors for magnetic targeting of aerosols.

Chen et al. [18] developed a two dimensional mathematical model using the Navier-Stokes equations and Maxwell's equations, to simulate magnetic targeting of magnetic particles using a magnetizable intravascular stent (MIS) inserted intro a blood vessel. They suggested that the radii of the MIS and its wire are important parameters for the collection efficiency. Grief and Richardson [32] conducted a theoretical analysis of the targeted drug delivery using magnetic particles and proposed a two-dimensional network model. In their model, the motion of fluid is described by Poiseuille flow, while the motion of the magnetic particles, due to balancing hydrodynamic and magnetic force, is governed by an advection-diffusion equation for the particle concentration. They found that drug targeting can be achieved by pulling magnetic particles to the edge of the vessel, and that the use of magnetically targeted drug delivery with an externally applied magnetic field is appropriate only for targets close to the surface of the body.

In 2007, Aviles [6] et al proposed a new approach of magnetic drug targeting

by using ferromagnetic particles as seeds to collect magnetic drug carrier particles at a specific site in the body. They used the Navier-Stokes equations to model the fluid flow, and the Maxwell equations to capture the magnetic potentials, and the force balance equation to calculate the motion of the carrier particles. The magnetic particle-particle interactions were neglected. The numerical results show that using the ferromagnetic seeds increases the performance of the magnetic drug targeting determined by the capture cross section.

Furlani and Furlani [27] developed a mathematical model based on the magnetic force, the drag force under the Stokes flow and the motion of magnetic particles for magnetic drug delivery in microvessels. They derived analytical expressions for the prediction of particle trajectory and the volume fraction of magnetic particles required to ensure capture of the particle, which is conversely proportional to the square of the radius of particles. Chertok et al. [20] used a simple mathematical model for the magnetohydrodynamic problem to distinguish the tumor brain from healthy brain by using magnetic nanoparticles and an external magnet. The prediction results were confirmed by the in vivo ratio of nanoparticle capture in bearing rats. In 2008, Chen [17] et al. developed a high-gradient magnetic separator to improve magnetic particle separation from blood flow in magnetic targeting application by introducing an array of capillary tubing and ferromagnetic wires which was immersed in an external magnetic field from two permanent magnets. They used a three dimensional finite element model, based on the equations similar to those in [18], to investigate the effect of the tubing-wire configurations. The numerical results show that an optimal design is to have bi-directionally alternating wires and tubes.

2.3 Modelling of Fluid Flow

Fluid dynamics involves the study of fluids in motion. More specifically, it concerns the kinematics of the flow field, and the stress distribution throughout the field. Based on the compressibility, fluids can be classified into compressible fluids and

incompressible fluids. Based on the constitutive equations, fluids can be categorized into three types: non-viscous, Newtonian, and non-Newtonian.

For most problems, liquids can be treated as incompressible fluids, and in general, gasses except low speed gas flows must be considered as compressible fluids. Furthermore, many common fluids, such as air and water, can be modelled as Newtonian fluids.

The governing equations of the flow of an incompressible Newtonian fluid consists of the equations of motion

$$\frac{\partial \sigma_{ij}}{\partial x_j} + \rho_f X_i = \rho_f \frac{Du_i}{Dt}, \tag{2.27}$$

the equation of continuity

$$\text{div}(\mathbf{u}) = \frac{\partial u_j}{\partial x_j} = 0, \tag{2.28}$$

and the constitutive equations

$$\sigma_{ij} = -p\delta_{ij} + 2\mu d_{ij}, \tag{2.29}$$

where $\dfrac{Du_i}{Dt} = \dfrac{\partial u_i}{\partial t} + u_j \dfrac{\partial u_i}{\partial x_j}$ is the material derivative, σ_{ij} are the components of stress tensor, ρ_f is the density of fluid, X_i are the components of body force in the x_i direction, δ_{ij} is the Kronecker symbol, u_i are the velocity of fluids in the x_i direction, p is the pressure, μ is the viscosity of fluid, and d_{ij} are the components of the rate of deformation (also known as strain rate) and is related to the velocity by

$$d_{ij} = \frac{1}{2}\left(\frac{\partial u_i}{\partial x_j} + \frac{\partial u_j}{\partial x_i}\right).$$

The above equations are all field equations which must be satisfied at all points within a continuum. To solve the above equations, substituting (2.33) into (2.27), we obtain

$$\rho_f \frac{Du_i}{Dt} = \rho_f X_i - \frac{\partial p}{\partial x_j}\delta_{ij} + \mu\left(\frac{\partial^2 u_i}{\partial x_j \partial x_j} + \frac{\partial^2 u_i}{\partial x_i \partial x_j}\right). \tag{2.30}$$

Using the continuity equation (2.28), we have

$$\frac{\partial^2 u_i}{\partial x_i \partial x_j} = \frac{\partial}{\partial x_i}\left(\frac{\partial u_j}{\partial x_j}\right) = 0,$$

and thus equation (2.30) becomes

$$\frac{Du_i}{Dt} = X_i - \frac{1}{\rho_f}\frac{\partial p}{\partial x_i} + \frac{\mu}{\rho_f}\nabla^2 u_i, \tag{2.31}$$

which are the so-called Navier-Stokes equations for incompressible Newtonian fluids. It should be noted that the Navier-Stokes equations for other kinds of fluids can be derived using the same process but with different constitutive equations. The Navier-Stokes equations (2.31) together with the continuity equation (2.28) constitute a system of four partial differential equations for unknown variables u, v, w, and p and thus are solvable in principle. These four partial differential equations define all possible motions of an incompressible Newtonian fluid. The feature which distinquishes one flow situation from another is the nature of the boundary conditions satisfied by the velocity field $\mathbf{u}$ and p.

In historical development of fluid theories and simulations, many studies have shown that fluids behave approximately like Newtonian fluid for which the shear stress in fluid is linearly proportional to the deformation rate, namely

$$\mu = \text{constant}. \tag{2.32}$$

However, most fluids are non-Newtonian, that is, the shear stress is related to the deformation rate nonlinearly by

$$\sigma_{ij} = -p\delta_{ij} + 2\mu(\dot{\gamma})d_{ij}, \tag{2.33}$$

where $\dot{\gamma}$ is the shear rate. Many non-Newtonian models for fluids have been suggested. Each model can be used to describe different fluid behaviour and contains different parameters. For bloods, a summary of non-Newtonian models of blood viscosity including the model parameters is given in [42], as in Table 2.1.

Many studies have been carried out to study the non-Newtonian behaviour of fluid and many models have been developed including, for example, the Carreau model, the Power-law model, the Casson model, and the generalized Power-law model. Mooney and Black [56] investigated the flow of raw rubber in extrusion operations. Both two and three dimensional flows were investigated. It was concluded that the non-Newtonian model was in a good agreement with Nadai's law of

Table 2.1: Blood viscosity models, μ , given in Poise (P) as a function of strain rate, $\dot{\gamma}$, given in s^{-1} [42].

Blood model	Effective viscosity μ
Newtonian	$\mu = 0.0345$ P
Carreau	$\mu = \mu_\infty + (\mu_0 - \mu_\infty)[1 + (\lambda\dot{\gamma})^2]^{(n-1)/2}$ where $\mu_0 = 0.56$ P,$\mu_\infty = 0.0345$ P, $\lambda = 3.313s$ and $n = 0.3568$
Walburn-Schneck	$\mu = C_1 e^{C_2 H}[e^{C_4(TPMA/H^2)}](\dot{\gamma})^{-C_3 H}$, where $C_1 = 0.00797, C_2 = 0.0608$, $C_3 = 0.00499, C_4 = 14.585lg^{-1}$, $H = 40\%$ and $TPMA = 25.9gl^{-1}$
Power Law	$\mu = \mu_0(\dot{\gamma})^{n-1}$ where $\mu_0 = 0.035$ and $n = 0.6$
Casson	$\mu = [(\eta^2 J_2)^{1/4} + 2^{-1/2}\tau_y^{1/2}]^2 J_2^{-1/2}$, where $\lvert\dot{\gamma}\rvert = 2\sqrt{J_2}, \tau_y = 0.1(0.625H)^3$, $\eta = \eta_0(1-H)^{-2.5}$ with $\eta_0 = 0.012$ P and $H = 0.37$
Generalised Power Law	$\mu = \lambda\lvert\dot{\gamma}\rvert^{n-1}$, $\lambda(\dot{\gamma}) = \mu_\infty + \Delta\mu \exp[-(1 + \frac{\lvert\dot{\gamma}\rvert}{a}) \exp(\frac{-b}{\lvert\dot{\gamma}\rvert})]$, $n(\dot{\gamma}) = n_\infty - \Delta n \exp[-(1 + \frac{\lvert\dot{\gamma}\rvert}{c}) \exp(\frac{-d}{\lvert\dot{\gamma}\rvert})]$, where $\mu_\infty = 0.035, n_\infty = 1.0, \Delta\mu = 0.25$, $\Delta n = 0.45, a = 50, b = 3, c = 50$ and $d = 4$

steady creep. Ali and Hayat [3] employed the Carreau model to study the peristaltic mechanism of a non-Newtonian fluid in an asymmetric channel. A perturbation technique was used to derive solutions in terms of power of a small Weissenberg number. Batra and Jena [8] studied the flow of a non-Newtonian fluid through a curved blood vessel using the Casson model. It was concluded that the ratio of the friction factor for the fluid in a curved tube to that in a straight tube depends on the Dean number and yield number.

Buick [11] studied the flow of a non-Newtonian fluid in a single-screw extruder using the power-law model. The lattice-Boltzmann method was used to simulate the behaviour of fluid flow. It was reported that the non-Newtonian model has an effect on the behaviour of the flow. Mandal et al. [52] investigated the flow of a non-Newtonian fluid through a simplex atomizer by simulating the transient flow of a viscous power-law fluid in the simplex atomizer using the volume-of-fluid method. It is found that the varying of power law index has no influence on the problem parameters including the angle and discharge coefficient. Mangadoddy et al. [53] investigated the flow of an incompressible non-Newtonian fluid in crossing over a bank of circular cylinders by using a power-law model. It is found that the Nusselt number depends on the Reynolds number, Prendtl number or Peclet number, power law index and the voidage of tube banks. Ismail et al. [41] studied blood flow in a tapered stenotic artery using the generalised power-law model. A finite difference scheme was used to simulate the behaviour of blood flow. They reported that the model showed lower values of the axial velocity profiles, flow rate, and wall shear stress, and higher values of the resistive impedances, compared with the Newtonian model. Soh and Mureithi [73] studied the flow of a non-Newtonian fluid down a heated inclined plane using the power-law temperature-dependent viscosity. The exact solutions were obtained using Bessel functions. The numerical solutions showed that the Froude number had significant effects on the flow velocity and temperature.

Gao and Wang [29] theoretically presented a mathematical model to study the incompressible non-Newtonian fluid using the generalized power-law model. A

similarity solution was detained using a perturbation technique and the Schander's fixed point theorem. The asymptotic behaviour of the solutions was also investigated.

2.4 Modelling of Particle-fluid Flow

Here we consider the cases where fluids adhere to rigid, but possible moving, surfaces bounding the fluids. It is evident that on a rigid surface, the normal component of the fluid velocity must be the same as that of the rigid surfaces, as fluids cannot penetrate the solid. For the tangential component of fluid velocity, two different boundary conditions may be used: no-slip condition and slip condition. For the no-slip condition, it is assumed that the tangential velocity component is likewise the same as that of the rigid surface. For the slip condition, it is assumed that slip can occur between the fluid and the rigid body. It has been found that the no-slip condition accords with experimental observation on most real materials.

Various mathematical models and numerical algorithms for the motion of particles in fluids have been developed. The numerical methods can be divided into three types including the continuum theory, the Lagrangian numerical simulation (LNS), and the direct numerical simulation (DNS). Based on these approaches, many research has been done to simulate the behaviour of particle flow in fluid.

The DNS approach is able to fully couple the motion of fluid flow and particles. In this method, various numerical methods have been developed. The first method is the Arbitary Lagrangian-Eulerian method (ALE). Takashi and Hughes [78] studied the vibration of a circular cylinder in a circular domain filled with a viscous fluid. In the ALE method, the material time derivative of a physical property φ is given by

$$\dot{\varphi} = \varphi' + c_i \varphi_{,i}, \tag{2.34}$$

where φ' is the referential time derivative keeping coordinates in the referential domain constant, and c_i is the convective velocity given by

$$c_i = u_i - \hat{u}_i, \tag{2.35}$$

where u_i is the material velocity and $\hat{u}_i$ is the mesh velocity. Applying the convective velocity to the equations of fluid motion, the ALE description of the Navier-Stokes equations and the continuity equation is given by

$$\begin{aligned} \rho u_i' + \rho(u_j - \hat{u}_j)\frac{\partial u_j}{\partial x_j} &= \frac{\partial \tau_{ij}}{\partial x_j} + f_i, \text{ in } \Omega_F(t), \\ \frac{\partial u_i}{\partial x_i} &= 0, \text{ in } \Omega_F(t), \end{aligned} \tag{2.36}$$

where u_i is the velocity vector of the fluid, ρ is the density, τ_{ij} is the stress tensor, and f_i is the body force vector. The fluid motion is described in the moving spatial domain $\Omega_F(t)$, while the domain occupied by the moving rigid body is denoted by $\Omega_G(t)$. The interface $\Gamma_I(t)$ between $\Omega_F(t)$ and $\Omega_G(t)$ moves as the domain $\Omega_G(t)$ changes its position. The boundary condition consists of two parts given by

$$\begin{aligned} u_i &= g_i \text{ on } \Gamma_g, \\ t_i &= \tau_{ij} n_j = h_i \text{ on } \Gamma_h, \end{aligned} \tag{2.37}$$

where t_i is the traction, n_i is the unit outward normal vector to Γ_h, and both g_i and h_i are specified functions of space and time. With the no-slip condition on the moving interface $\Gamma_I(t)$, the unknown velocity u_i^I on $\Gamma_I(t)$ can be determined by

$$u_i^I = \hat{u}_i. \tag{2.38}$$

Based on this ALE formulation, Hu [36] simulated the Poiseuille flow of solid-fluid mixtures of 400 solid particles in fluid contained in a vertical channel.

The second method in DNS is the lattice-Boltmann method (BLM). Ladd [44] developed the method to solve the Navier-Stokes equations and gave some simple examples in solving the Stokes equations. In this method, the mass density ρ, the momentum density $j = \rho u$, and the momentum flux Π are given by

$$\begin{aligned} \rho &= \textstyle\sum_i n_i, \\ j &= \textstyle\sum_i n_i c_i, \\ \Pi &= \textstyle\sum_i n_i c_i c_i, \end{aligned} \tag{2.39}$$

where $n_i(r,t)$ is the continuous velocity distribution function of the discretized quantities $r, t,$ and c_i, where r is the number of particles at a particular node of the lattice at time t with velocity c_i.

In 2000, Pereira [62] studied the fluid-particle flow problem using the finite difference model. The motion of spherical and cylindrical particles in steady state Newtonian and non-Newtonian fluid flow inside a tube was investigated by determining the ratio between the additional force and the drag force on the particle, and the ratio between the additional force on the duct wall and the drag force on the particles. In 2004, Longest et al. [50] presented a mathematical model based on the Eulerian-Lagrangian method to simulate the trajectories of discrete blood particles including particle-wall interactions and the quantification of near-wall stasis, using the near-wall residence time model. They used the CFX finite volume package to apply a femoral bypass end-to-side anastomosis as a real model geometry. The numerical results show that an extended form of the particle trajectory equation is needed when particle-wall interaction terms dominate.

In 2006, Bikard et al. [9] studied a three dimensional mathematical model for the fluid flow around a rigid sphere suspended in a Newtonian matrix and submitted to a simple shear. They used the Rem3D finite element software to calculate the flow and the hydrodynamic stresses around the particle. The numerical results agree with the results from the direct calculation, and the matrix has significant effects on the proximity of the matrix walls toward the particles. In 2007, Al Quddus et al. [1] developed a mathematical model based the Navier-Stokes equations and an arbitary Lagragian Eulerian method and used the finite element approach to study the motion of particles in fluids in infinite and finite length channels. The simulation results are in good agreement with other analytical and numerical results for the Stokes hindrance factors in capillary flows. A double exponential relation between the wall correction factors and particle to channel radii ratio was obtained. They also investigated the effect of entrance and exit of an open channel, and a capped end of a channel.

2.5 Concluding Remarks

A large number of studies related to the fluid flow and particle flow in fluid in microscale have been carried out over the last few decades in order to understand the interaction between fluids and particles. Many mathematical models have been used to simulate the fluid-particle flow. A large amount of work have also been conducted to study the effect of magnetic fields to fluid flow. This research will focus on the fluid-particle flow through microchannels under magnetic fields.

Chapter 3

Transient Flow of Fluids through Micro-annuals

3.1 General Overview

From the fundamental principles of continuum mechanics, the flow of incompressible Newtonian fluids is governed by the continuity equation, the Navier-Stokes equations and a set of boundary conditions. Traditionally the so-called no-slip boundary condition is used, namely the fluid velocity relative to the solid is assumed to be zero on the fluid-solid interface [71]. However, evidences of slip of a fluid on a solid surface have been reported [63]. Chauveteau [16], Tuinier and Taniguchi [82], and Vargas and Manero [22] studied the flow of polymer solutions in porous media and showed that the apparent viscosity of the fluids near the wall is lower than that in the bulk and consequently the fluids can exhibit the phenomenon of apparent slip on the wall. More recently, experiments in micrometer scale and molecular dynamic simulations showed that the flow of fluids in microsystems is granular and slip can occur on the fluid-solid interface [14, 15, 77, 91, 95]. Hence, under certain conditions such as those investigated in [81, 85], the no-slip condition is not acceptable for fluid flows in microchannels. On the other hand, many experimental results have provided evidences to support the Navier slip condition [38, 63, 93], namely the fluid velocity component tangential to the solid surface, relative to the solid surface, is proportional to the shear stress on the fluid-solid in-

terface. The proportionality is called the slip length which describes the *slipperiness* of the surface [45, 93]. Some attempts have also been made to derive alternative formulae for the determination of the slip length [79], and to use nanotechnologies for the surface treatment of microchannels so as to achieve large slip for maximizing the transport efficiency of fluids through microchannels. Based on the nature of boundary slip of microflows, we will use the Navier slip condition for fluid flow in micro-annuals.

Over the last couple of decades, many investigations have been made to study various flow problems of Newtonian and non Newtonian fluids with the no-slip boundary condition or a slip boundary condition [13, 21, 23, 46, 54, 61, 67, 68, 81, 94]. Although exact and numerical solutions to many flow problems of Newtonian fluids under the no-slip assumption have been obtained and are available in literature [71, 87, 88, 89], very few exact solutions for the slip case are available in literature. Recently, some steady state slip solutions for the flows through a pipe, a channel and an annulus have been obtained [55, 92]. An exact solution for the transient flow through microtubes has also been derived and discussed in the paper [90].

Motivated by the previous work, we study the transient flow of an incompressible Newtonian liquid through a micro-annual with a slip boundary in this paper. The work is basically an extension of our previous work in [90]. Here we should address that micro-devices with annulus geometry, such as microreactor with multicylindrical mixer structure [34], are extremely difficult to fabricate using current microfabrication technology. The rest of the paper is organized as follows. In the following section, we first define the problem and then present its mathematical formulation. In section 3, we solve the underlying boundary value problem to derive the exact solution for the velocity field and show that the solution includes some existing known solutions as special cases. In section 4, we derive exact solutions for the flow rate, the rate of deformation tensor and the stress field in the fluid using the exact solution of velocity field derived in section 3. In section 5, an analysis is carried out to study the influence of the slip parameter on the flow behaviour. Finally a conclusion is given in section 6.

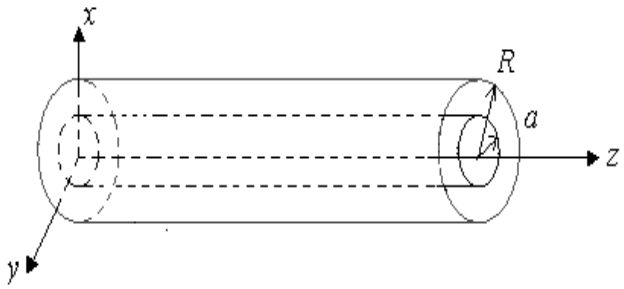

Figure 3.1: The coordinate system used .

3.2 Governing Equations

Consider the transient flow of an incompressible Newtonian liquid through a circular annual of inner radius a and outer radius R with the z-axis being in the axial direction as shown in Figure 3.1. We limit our analysis to fully developed flow and assume that the slip length does not change along the flow. The field equations governing the flow include the continuity equation and the Navier-Stokes equations. As the flow is axially symmetric and fully developed, there is no swirling flow and the velocity components in the radial and transverse directions vanish, namely $\mathbf{v} = (v_r,\ v_\theta,\ v_z) = (0,\ 0,\ u)$. Thus, from the continuity equation and the Navier-Stokes equations, as shown in [90], u must satisfy the following equation

$$\frac{\mu}{\rho}\left(\frac{\partial^2 u}{\partial r^2} + \frac{1}{r}\frac{\partial u}{\partial r}\right) - \frac{\partial u}{\partial t} \ = \ \frac{1}{\rho}\frac{\partial p}{\partial z}. \tag{3.1}$$

Since a wide range of functions can be expressed in terms of Fourier series, in this work, we consider the fluid flow driven by the pressure field with a pressure gradient that can be expressed by the Fourier series

$$\frac{\partial p}{\partial z} \ = \ a_0 + \sum_{n=1}^{\infty}[a_n cos(n\omega t) + b_n sin(n\omega t)] := q(t). \tag{3.2}$$

To completely define the problem, the field equations must be supplemented by the boundary condition. In this work, we use the Navier slip boundary condition. That is, on the solid-fluid interfaces $r = a$ (inner surface) and $r = R$ (outer surface), the axial fluid velocity, relative to the solid surface, is proportional to the shear stress

on the interface. For Newtonian fluids, the shear stress is related to the shear strain rate by $\sigma_{rz} = \mu\frac{\partial u}{\partial z}$ where μ is the fluid viscosity. Thus, for the case where the rigid micro-annulus is fixed spatially, the Navier slip condition can be written in the form of

$$u(a,t) \;=\; \pm l_1 \frac{\partial u}{\partial r}(a,t), \quad u(R,t) \;=\; \pm l_2 \frac{\partial u}{\partial r}(R,t), \tag{3.3}$$

where l_1 and l_2 denote the slip parameters of the inner surface and the outer surface respectively. In this study, we assume that the slip parameter does not change along the flow. The signs for the terms on the right hand sides of the above equations have been discussed by various authors. In literature, all the four possible cases are considered and the physically feasible cases are determined based on the solution derived. Here, we give a different method for choosing the sign for the terms on the right hand sides of the equations in (3.3) without the need of finding the solution first, as detailed below.

From the physics of fluids, when the fluid moves relative to the solid surface in the tangential direction of the solid surface, the relative movement of the fluid particles will be restricted by a resistance force acting on the opposite direction of the relative movement. Let the unit outward normal vector of the surface S of the fluid is $\mathbf{n} = (n_1, n_2, n_3)$, and the positive tangential direction is $\mathbf{t} = (t_1, t_2, t_3)$. Suppose the stress tensor in the fluid is σ_{ij}, then the surface traction on S is $X_i = \sigma_{ji} n_j$ which has the tangential component $f_t = X_i t_i = \sigma_{ji} n_j t_i$, where we have used the index notation with the repeated literal indexes representing summation over the index range. On the other hand, the velocity component of the fluid relative to the solid surface on the tangential direction is $v_t - v_{st} = (v_i - v_{si})t_i$. Hence the Navier type boundary condition for Newtonian fluids can be written as

$$v_t - v_{st} \;=\; -\frac{l f_t}{\mu} \quad \texttt{or} \quad (v_i - v_{si})t_i \;=\; -\frac{l(\sigma_{ji} n_j t_i)}{\mu}. \tag{3.4}$$

The negative sign in the above equations is to indicate that the direction of the relative tangential velocity is opposite to the surface traction force exerted on the fluid by the solid surface. Now for our problem in the (r, θ, z) system, $\mathbf{v} = (0, 0, u)$, $\mathbf{v}_s = (0,\ 0,\ 0)$. For the outer surface $r = R$, $\mathbf{n} = (1, 0, 0)$ and $\mathbf{t} =$

$(0,0,1)$, and so $v_t - v_{st} = v_i t_i = u$ and $f_t = \sigma_{rz} = \mu\frac{\partial u}{\partial r}$ and consequently $(3.3)_2$ for the outer surface takes the following form

$$u(R,t) \;=\; -l_2\frac{\partial u}{\partial r}(R,t). \tag{3.5}$$

For the inner surface $r = a$, $\mathbf{n} = (-1,0,0)$ and $\mathbf{t} = (0,0,1)$, and so $v_t - v_{st} = v_i t_i = u$ and $f_t = -\sigma_{rz} = -\mu\frac{\partial u}{\partial r}$ and consequently $(3.3)_1$ for the inner surface takes the following form

$$u(a,t) \;=\; l_1\frac{\partial u}{\partial r}(a,t). \tag{3.6}$$

It should also be addressed here that for $l_i = 0$, conditions (3.5)-(3.6) reduce to the no-slip boundary condition; while, for $l_i \to \infty$, equations (3.5) and (3.6) give the surface traction condition for perfectly smooth surfaces, i.e, $\sigma_{rz}(a,t) = \sigma_{rz}(R,t) = 0$.

Remark 2.1 The formula (3.4) is more precise than (3.3) and is more suitable for application in numerical analysis.

3.3 Exact Solution for Velocity Field

To solve equation (3.1), firstly we use complex number to express the above Fourier series by exponential functions, namely

$$\frac{\partial p}{\partial z} \;=\; \mathtt{Re}\left(\sum_{n=0}^{\infty} c_n e^{in\omega t}\right), \tag{3.7}$$

where $c_n = a_n - b_n i$ and $e^{in\omega t} = cos(n\omega t) + isin(n\omega t)$.

From the linear property of equation (3.1), we have $u = \sum_{n=0}^{\infty}\mathtt{Re}(u_n)$, where u_n is defined by

$$\frac{\mu}{\rho}\left(\frac{\partial^2 u_n}{\partial r^2} + \frac{1}{r}\frac{\partial u_n}{\partial r}\right) - \frac{\partial u_n}{\partial t} \;=\; \frac{c_n}{\rho}e^{in\omega t}. \tag{3.8}$$

As in [90], let

$$u_n \;=\; f_n(r)e^{in\omega t}. \tag{3.9}$$

Then, we have

$$\frac{\mu}{\rho}\left(\frac{\partial^2 f_n}{\partial r^2}+\frac{1}{r}\frac{\partial f_n}{\partial r}\right)-in\omega f_n \;=\; \frac{c_n}{\rho}. \tag{3.10}$$

For $n=0$, equation (3.10) has the following general solution

$$f_0(r) \;=\; (A_1+A_2 lnr)+\frac{c_0}{4\mu}r^2. \tag{3.11}$$

For $n\geq 1$, equation (3.10) can be written as

$$\bar{r}^2\frac{\partial^2 f_n}{\partial \bar{r}^2}+\bar{r}\frac{\partial f_n}{\partial \bar{r}}+\bar{r}^2 f_n \;=\; \frac{c_n}{\beta_n^2\mu}\bar{r}^2, \tag{3.12}$$

where $\beta_n^2=n\beta^2$ in which $\beta^2=-\frac{\rho\omega}{\mu}i$, and $\bar{r}=\beta_n r$.

As the associated homogeneous equation is the zero-order Bessel equation, equation (3.12) has the following general solution

$$f_n \;=\; d_n J_0(\bar{r})+e_n Y_0(\bar{r})+\frac{c_n}{\beta_n^2\mu} \;=\; d_n J_0(\beta_n r)+e_n Y_0(\beta_n r)+\frac{c_n i}{\rho n\omega}, \tag{3.13}$$

where d_n and e_n are integration constants; J_0 and Y_0 denote the zero-order Bessel functions of the first kind and the second kind respectively. Thus, we have

$$\begin{array}{rcl} u=\sum_{n=0}^{\infty}\mathtt{Re}(u_n) & = & A_1+A_2\mathtt{ln}(r)+\frac{a_0}{4\mu}r^2 \\ & + & \sum_{n=1}^{\infty}\mathtt{Re}\left[\left(d_n J_0(\beta_n r)+e_n Y_0(\beta_n r)+\frac{c_n i}{\rho n\omega}\right)e^{in\omega t}\right], \end{array} \tag{3.14}$$

from which we obtain

$$\frac{\partial u}{\partial r}=A_2\frac{1}{r}+\frac{a_0}{2\mu}r-\mathtt{Re}\sum_{n=1}^{\infty}\left[d_n J_1(\beta_n r)+e_n Y_1(\beta_n r)\right]\beta_n e^{in\omega t}, \tag{3.15}$$

where, in the above formulation, we have used the identities

$$\frac{dJ_0(x)}{dx}=-J_1(x), \quad \frac{dY_0(x)}{dx} \;=\; -Y_1(x). \tag{3.16}$$

Substituting (3.14) and (3.15) into boundary conditions (3.5-3.6) yields

$$\begin{array}{c} \left(A_1+A_2 ln(a)+\frac{a_0}{4\mu}a^2-A_2\frac{1}{a}l_1-\frac{a_0}{2\mu}al_1\right)+\mathtt{Re}\sum_{n=1}^{\infty}[d_n J_0(\beta_n a)+e_n Y_0(\beta_n a) \\ +\frac{c_n i}{\rho n\omega}+l_1\beta_n d_n J_1(\beta_n a)+l_1\beta_n e_n Y_1(\beta_n a)]e^{in\omega t} \;=\; 0, \\ \left(A_1+A_2 ln(R)+\frac{a_0}{4\mu}R^2+A_2\frac{1}{R}l_2+\frac{a_0}{2\mu}Rl_2\right)+\mathtt{Re}\sum_{n=1}^{\infty}[d_n J_0(\beta_n R)+e_n Y_0(\beta_n R) \\ +\frac{c_n i}{\rho n\omega}-l_2\beta_n d_n J_1(\beta_n R)-l_2\beta_n e_n Y_1(\beta_n R)]e^{in\omega t} \;=\; 0. \end{array} \tag{3.17}$$

For the above equations to hold for any instant of time t, we require that

$$\begin{aligned}
&A_1 + A_2\left(ln(a) - \tfrac{1}{a}l_1\right) \;=\; -\tfrac{a_0}{4\mu}\left(a^2 - 2al_1\right),\\
&A_1 + A_2\left(ln(R) + \tfrac{1}{R}l_2\right) \;=\; -\tfrac{a_0}{4\mu}\left(R^2 + 2Rl_2\right),\\
&d_n[J_0(\beta_n a) + l_1\beta_n J_1(\beta_n a)] + e_n[Y_0(\beta_n a) + l_1\beta_n Y_1(\beta_n a)] \;=\; -\tfrac{c_n i}{\rho n\omega},\\
&d_n[J_0(\beta_n R) - l_2\beta_n J_1(\beta_n R)] + e_n[Y_0(\beta_n R) - l_2\beta_n Y_1(\beta_n R)] \;=\; -\tfrac{c_n i}{\rho n\omega}.
\end{aligned} \tag{3.18}$$

Solving the above system of equations for $A_1,\ A_2,\ d_n$ and e_n, and then submitting them into (3.14), we obtain

$$\begin{aligned}
u \;=\; &-\tfrac{a_0R^2}{4\mu}\left(1 - \left(\tfrac{r}{R}\right)^2 + \tfrac{2l_2}{R} + \tfrac{1-\left(\frac{a}{R}\right)^2+2\left(\frac{l_2}{R}+\frac{al_1}{R^2}\right)}{ln\frac{R}{a}+\frac{l_2}{R}+\frac{l_1}{a}}\left(ln\tfrac{r}{R} - \tfrac{l_2}{R}\right)\right)\\
&-\mathtt{Re}\textstyle\sum_{n=1}^{\infty}\tfrac{c_n i e^{in\omega t}}{\rho n\omega}\left\{\tfrac{N_1}{D}J_0(\beta_n r) + \tfrac{N_2}{D}Y_0(\beta_n r) - 1\right\},
\end{aligned} \tag{3.19}$$

where

$$\begin{aligned}
N_1 \;&=\; N_1(a,R,\beta_n,l_1,l_2) \;=\; Y_0(\beta_n R) - Y_0(\beta_n a) - [l_2Y_1(\beta_n R) + l_1Y_1(\beta_n a)]\beta_n,\\
N_2 \;&=\; N_2(a,R,\beta_n,l_1,l_2) \;=\; J_0(\beta_n a) - J_0(\beta_n R) + [l_1J_1(\beta_n a) + l_2J_1(\beta_n R)]\beta_n,\\
D \;&=\; D(a,R,\beta_n,l_1,l_2) \;=\; J_0(\beta_n a)Y_0(\beta_n R) - J_0(\beta_n R)Y_0(\beta_n a)\\
&\quad +[J_1(\beta_n a)Y_0(\beta_n R) - J_0(\beta_n R)Y_1(\beta_n a)]l_1\beta_n\\
&\quad +[J_1(\beta_n R)Y_0(\beta_n a) - J_0(\beta_n a)Y_1(\beta_n R)]l_2\beta_n\\
&\quad +[J_1(\beta_n R)Y_1(\beta_n a) - J_1(\beta_n a)Y_1(\beta_n R)]l_1l_2\beta_n^2.
\end{aligned} \tag{3.20}$$

Remark 3.1 If $l_1 = l_2 = 0$, solution (3.19) becomes

$$\begin{aligned}
u \;=\; &-\tfrac{a_0R^2}{4\mu}\left\{1 - \left(\tfrac{r}{R}\right)^2 + \left[1 - \left(\tfrac{a}{R}\right)^2\right]\tfrac{ln(r/R)}{ln(R/a)}\right\}\\
&-\mathtt{Re}\textstyle\sum_{n=1}^{\infty}\tfrac{c_n i e^{in\omega t}}{\rho n\omega}\left\{\tfrac{[Y_0(\beta_n R)-Y_0(\beta_n a)]J_0(\beta_n r)+[J_0(\beta_n a)-J_0(\beta_n R)]Y_0(\beta_n r)}{J_0(\beta_n a)Y_0(\beta_n R)-J_0(\beta_n R)Y_0(\beta_n a)} - 1\right\},
\end{aligned} \tag{3.21}$$

which is the solution for the traditional no-slip case [40].

Remark 3.2 If $a_0 = -A \in R,\ c_n = 0$ for all $n \geq 1,\ l_1/R = l_2/R = l,\ a = \kappa R,\ u = -v_z\frac{a_0R^2}{4\mu}$ then the solution reduces to a recent result given in equation (3.19) in reference [55].

3.4 Exact Solution of the Flow Rate and Stress Field

From the axial velocity solution (3.19), the flow rate can be determined as

$$Q(t) \;=\; \int_a^R 2\pi r u(r,t)\,dr \;=\; Q_0 + \sum_{n=1}^{\infty} Q_n, \tag{3.22}$$

where Q_0 and Q_n are respectively the flow rate corresponding to the constant component and the nth harmonic component of the pressure gradient and

$$\begin{aligned} Q_0 &= -\frac{a_0\pi R^4}{8\mu}\left\{\left[1-\left(\frac{a}{R}\right)^2\right]\left[1-\left(\frac{a}{R}\right)^2+\frac{4l_2}{R}\right]\right. \\ &\left.-\frac{1-\left(\frac{a}{R}\right)^2+2\left(\frac{l_2}{R}+\frac{al_1}{R^2}\right)}{ln\frac{R}{a}+\frac{l_2}{R}+\frac{l_1}{a}}\left[1-\left(\frac{a}{R}\right)^2+\frac{2l_2}{R}-\frac{2l_2a^2}{R^3}+2\left(\frac{a}{R}\right)^2 ln\frac{a}{R}\right]\right\}, \end{aligned} \tag{3.23}$$

$$Q_n = -\mathtt{Re}\left\{\left[\frac{N_1}{D}\int_a^R rJ_0(\beta_n r)\,dr+\frac{N_2}{D}\int_a^R rY_0(\beta_n r)\,dr-\frac{1}{2}(R^2-a^2)\right]\frac{2\pi c_n i e^{in\omega t}}{n\rho\omega}\right\}. \tag{3.24}$$

From the identities

$$\frac{d}{dx}[xJ_1(x)] = xJ_0(x), \qquad \frac{d}{dx}[xY_1(x)] = xY_0(x), \tag{3.25}$$

we have

$$\begin{aligned} \int_a^R rJ_0(\beta_n r)\,dr &= \frac{1}{\beta_n}[RJ_1(\beta_n R)-aJ_1(\beta_n a)], \\ \int_a^R rY_0(\beta_n r)\,dr &= \frac{1}{\beta_n}[RY_1(\beta_n R)-aY_1(\beta_n a)]. \end{aligned} \tag{3.26}$$

Thus, by substituting the above formula into (3.22), we have

$$\begin{aligned} Q_n &= -\mathtt{Re}\frac{2\pi c_n i e^{in\omega t}}{n\rho\omega}\left\{\frac{N_1}{\beta_n D}[RJ_1(\beta_n R)-aJ_1(\beta_n a)]\right. \\ &\left.+\frac{N_2}{\beta_n D}\left[RY_1(\beta_n R)-aY_1(\beta_n a)\right]-\frac{1}{2}(R^2-a^2)\right\}. \end{aligned} \tag{3.27}$$

Remark 4.1 From the above solution form, it is not immediately clear whether the transient flow rate increases as l_1 and/or l_2 increases, and thus we will study this in section 5.

The stress in the fluid is related to the velocity field by the following constitutive equations

$$\sigma = -pI+2\mu\mathbf{d}, \tag{3.28}$$

while the rate of deformation tensor is related to the velocity vector by

$$\mathbf{d} = \frac{1}{2}\left(\nabla\mathbf{v}+(\nabla\mathbf{v})^T\right), \tag{3.29}$$

where $\sigma \equiv (\sigma_{ij})$ and $\mathbf{d} = (d_{ij})$ denote respectively the second order stress tensor and the rate of deformation tensor, I is an identity matrix. As $\mathbf{v} = (0,\ 0,\ u(r,t))$, we have

$$\mathbf{d} = \frac{1}{2}\begin{pmatrix} 0 & 0 & \partial u/\partial r \\ 0 & 0 & 0 \\ \partial u/\partial r & 0 & 0 \end{pmatrix}. \tag{3.30}$$

From the above formula and using (3.19), we obtain $d_{rr} = d_{\theta\theta} = d_{zz} = d_{r\theta} = d_{\theta z} = 0$ and

$$d_{rz} = -\frac{a_0 R}{8\mu}\left[-\frac{2r}{R} + \frac{1-\left(\frac{a}{R}\right)^2+2\left(\frac{l_2}{R}+\frac{al_1}{R^2}\right)}{ln\frac{R}{a}+\frac{l_2}{R}+\frac{l_1}{a}}\frac{R}{r}\right]$$
$$+\mathrm{Re}\sum_{n=1}^{\infty}\frac{c_n i e^{in\omega t}}{2\rho n\omega}\left\{\frac{N_1(a,R,\beta_n,l_1,l_2)}{D(a,R,\beta_n,l_1,l_2)}\beta_n J_1(\beta_n r) + \frac{N_2(a,R,\beta_n,l_1,l_2)}{D(a,R,\beta_n,l_1,l_2)}\beta_n Y_1(\beta_n r)\right\}. \tag{3.31}$$

Hence from the constitutive equations (3.28), we obtain

$$\sigma_{rr} = \sigma_{\theta\theta} = \sigma_{zz} = -p = q(t)z + p_0(t),\ \sigma_{r\theta} = \sigma_{\theta z} = 0$$
$$\sigma_{rz} = -\frac{a_0 R}{4}\left[-\frac{2r}{R} + \frac{1-\left(\frac{a}{R}\right)^2+2\left(\frac{l_2}{R}+\frac{al_1}{R^2}\right)}{ln\frac{R}{a}+\frac{l_2}{R}+\frac{l_1}{a}}\frac{R}{r}\right]$$
$$+\mathrm{Re}\sum_{n=1}^{\infty}\frac{c_n \mu i e^{in\omega t}}{\rho n\omega}\left\{\frac{N_1(a,R,\beta_n,l_1,l_2)}{D(a,R,\beta_n,l_1,l_2)}\beta_n J_1(\beta_n r) + \frac{N_2(a,R,\beta_n,l_1,l_2)}{D(a,R,\beta_n,l_1,l_2)}\beta_n Y_1(\beta_n r)\right\}, \tag{3.32}$$

where $q(t)$ is as given in (3.2) while $p_0(t)$ is arbitrary and can be chosen to meet certain pressure condition.

3.5 Influence of Boundary Slip

With the exact solutions obtained in the previous sections, in this section, we discuss the influences of the slip length on velocity, flow rate and stresses in the fluid. As the solution for a general pressure field given by (3.2) is the superposition of the solution due to the constant pressure gradient and the solutions due to the sine and cosine wave form pressure gradients, without loss of generality, we consider here two different cases of driving pressure fields in this discussion. The first case is for a pressure field with a constant pressure gradient, while the second one is for a pressure field with a sine wave form pressure gradient. For convenience in the discussion, we introduce the following dimensionless variables

$$r^* = \frac{r}{R},\ k = \frac{a}{R},\ l = \frac{l_2}{R},\ \lambda = \frac{l_1}{l_2},\ t^* = \frac{\omega t}{2\pi},\ \beta^* = \beta R. \tag{3.33}$$

Case 1: $\frac{dp}{dz} = a_0$.

For this case, $c_n = 0$ for all $n \geq 1$. Then from (3.19), (3.22)-(3.23) and (3.32),

we obtain the following normalized velocity, normalized flow rate and shear stress

$$u^* = -\frac{4\mu}{a_0 R^2}u = \left[1 - r^{*2} + 2l + \frac{1-k^2+2(1+k\lambda)l}{ln\frac{1}{k} + \left(1+\frac{\lambda}{k}\right)l}(ln\, r^* - l)\right], \quad (3.34)$$

$$\begin{aligned} Q^* &= -\tfrac{8\mu}{a_0\pi R^4}Q \\ &= (1-k^2)(1-k^2+4l) - \tfrac{1-k^2+2(1+k\lambda)l}{ln\frac{1}{k}+\left(1+\frac{\lambda}{k}\right)l}\left[(1-k^2)(1+2l) + 2k^2 ln(k)\right], \end{aligned} \quad (3.35)$$

$$\sigma^*_{rz} = -\frac{4}{a_0 R}\sigma_{rz} = \left[-2r^* + \frac{1-k^2+2(1+k\lambda)l}{ln\frac{1}{k} + \left(1+\frac{\lambda}{k}\right)l}\frac{1}{r^*}\right]. \quad (3.36)$$

It should be addressed here that for $l = 0$, the solution (34) reduces to the solution for the no-slip case [40]. To study the influence of l on the velocity, we examine the derivative of u^* with respect to l. From (3.34), we have

$$\frac{du^*}{dl} = \left[a(k,\lambda,r^*) + b(k,\lambda)l + c(k,l)l^2\right]\left[ln\frac{1}{k} + \left(1+\frac{\lambda}{k}\right)l\right]^{-2}, \quad (3.37)$$

where

$$a(k,\lambda,r^*) = (2ln(k)+1-k^2)(ln(k)-ln(r^*)) - \lambda k ln(r^*)(2ln(k)+\tfrac{1}{k^2}-1),$$

$$b(k,\lambda) = 4\lambda ln(k)(k-\tfrac{1}{k}),\ c(k,\lambda) = 2\lambda(\tfrac{1}{k}-k)(1+\tfrac{\lambda}{k}).$$

As $\lambda > 0, 0 < k < 1$, and $k \le r^* \le 1$, we can easily prove that $a > 0,\ b > 0$ and $c > 0$, and hence $\frac{du^*}{dl} > 0$ for $l \ge 0$, which means that the velocity is a monotonically increasing function of l. Similarly, we can also prove that the flow rate also increases monotonically as l increases from zero. Also, for $l >> max\left\{1, ln\frac{1}{k}\right\}$, from (35), we have

$$\frac{\partial Q*}{\partial l} \approx 4\left(1-k^2\right)\left(1 - \frac{1+k\lambda}{1+\lambda/k}\right) > 0,$$

which indicates that Q* increases almost linearly with increasing l when l is sufficient large.

To further demonstrate the characteristics of the variation of the flow rate with l and k, we show the solution (3.35) graphically in Figure 2 for the case where both

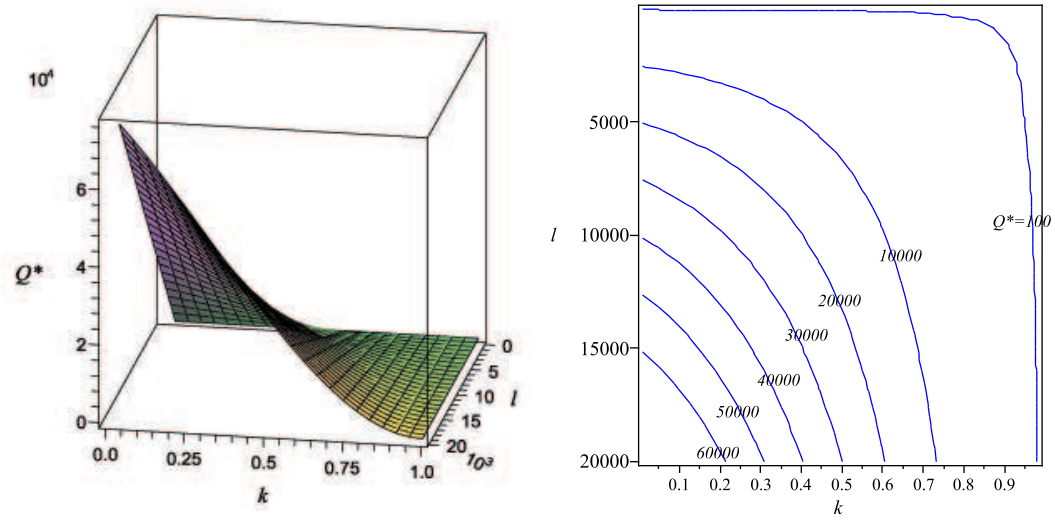

(a) (b)

Figure 3.2: Variation of the flow rate with l and k obtained from solution (3.35) with $\lambda = 1$: (a) 3D graph for $Q^*(k, l)$; (b) contour plot of $Q^*(k, l)$ on (k, l) plane.

the inner and outer surfaces have the same smoothness, i.e. $\lambda = 1$. The result shows that there exists different (l, k) parameter designs for obtaining a given fixed flow rate, which opens a way for the optimal design of the annual. The result also shows that the influence of l on the flow rate is more significant for lower k values. It is also interesting to note that the velocity field in the annual is not a simple superposition of the no-slip solution and a rigid body translation, as is in the circular microtubes [90].

Case 2: $\frac{dp}{dz} = b_1 sin(\omega t)$.

For this case, $a_0 = 0,\ c_1 = -b_1 i,\ c_n = 0$ for all $n \geq 2$. As $\beta^2 = -\frac{\rho\omega}{\mu} i = \frac{\rho\omega}{\mu} e^{-\pi i/2}$, we have

$$\beta = \sqrt{\frac{\rho\omega}{2\mu}}(1-i) = \frac{\bar{\beta}}{R}(1-i),\quad \frac{1}{\beta} = \frac{R}{2\bar{\beta}}(1+i),\quad \beta^* = \bar{\beta}(1-i), \tag{3.38}$$

where $\bar{\beta} = R\sqrt{\frac{\rho\omega}{2\mu}}$ is a dimensionless parameter. Then, using the dimensionless variables in (3.33), we have from (3.19), (3.27) and (3.32) that

$$\begin{aligned} u^* &= -\tfrac{\rho}{b_1} u, \\ &= \mathrm{Re}\left\{ \left[\tfrac{N_1}{D} J_0(\beta^* r^*) + \tfrac{N_2}{D} Y_0(\beta^* r^*) - 1 \right] \tfrac{1}{\omega} e^{2\pi t^* i} \right\}, \end{aligned} \tag{3.39}$$

$$
\begin{aligned}
Q^* &= -\tfrac{\rho}{2\pi b_1 R^2} Q_n, \\
&= \mathtt{Re}\left\{ \left[\tfrac{N_1}{\beta^* D}[J_1(\beta^*) - kJ_1(\beta^* k)] + \tfrac{N_2}{\beta^* D}[Y_1(\beta^*) - kY_1(\beta^* k)] \right.\right. \\
&\quad \left.\left. -\tfrac{1}{2}(1-k^2)\right] \tfrac{1}{\omega} e^{2\pi t^* i} \right\}, \qquad (3.40) \\
\sigma^*_{rz} &= \tfrac{\rho R}{\mu b_1}\sigma_{rz}, \\
&= \mathtt{Re}\left\{ \left[\tfrac{N_1}{D}\beta^* J_1(\beta^* r^*) + \tfrac{N_2}{D}\beta^* Y_1(\beta^* r^*) \right] \tfrac{1}{\omega} e^{2\pi t^* i} \right\}, \qquad (3.41)
\end{aligned}
$$

where

$$
\begin{aligned}
N_1 &= Y_0(\beta^*) - Y_0(\beta^* k) - [Y_1(\beta^*) + \lambda Y_1(\beta^* k)] l\beta^*, \\
N_2 &= J_0(\beta^* k) - J_0(\beta^*) + [\lambda J_1(\beta^* k) + J_1(\beta^*)] l\beta^*, \\
D &= J_0(\beta^* k) Y_0(\beta^*) - J_0(\beta^*) Y_0(\beta^* k) \\
&\quad + [J_1(\beta^* k) Y_0(\beta^*) - J_0(\beta^*) Y_1(\beta^* k)] \lambda l\beta^* \\
&\quad + [J_1(\beta^*) Y_0(\beta^* k) - J_0(\beta^* k) Y_1(\beta^*)] l\beta^* \\
&\quad + [J_1(\beta^*) Y_1(\beta^* k) - J_1(\beta^* k) Y_1(\beta^*)] \lambda l^2 \beta^{*2}.
\end{aligned} \qquad (3.42)
$$

For convenience in discussion, let

$$
\frac{N_1}{\omega\beta^* D}[J_1(\beta^*) - kJ_1(\beta^* k)] + \frac{N_2}{\omega\beta^* D}[Y_1(\beta^*) - kY_1(\beta^* k)] \;:=\; a + bi, \qquad (3.43)
$$

then equation (40) can be written as

$$
Q^* \;=\; Q^*_m(k,l)\; sin(2\pi t^* + \phi(k,l)),
$$

where $Q^*_m(k,l)$ and $\phi(k,l)$ are respectively the amplitude and phase angle of the normalized transient flow rate defined by

$$
\begin{aligned}
Q^*_m(k,l) &= \left(\left(a - \tfrac{1}{2\omega}(1-k^2)\right)^2 + b^2 \right)^{1/2}, \\
\phi(k,l) &= \mathtt{arctan}\left(\tfrac{\frac{1}{2\omega}(1-k^2) - a}{b} \right).
\end{aligned} \qquad (3.44)
$$

In the following, we first study the influence of the angular frequency ω on the amplitude of the transient flow rate $Q^*_m(k,l)$, and compare the transient solutions with the quasi steady-state solution which is obtained by neglecting the time derivative term in equation (1) to yield

$$
u^* = -\frac{\rho}{b_1} u = \frac{\rho R^2}{4\mu} \left[1 - r^{*2} + 2l + \frac{1 - k^2 + 2(1+k\lambda)l}{ln\frac{1}{k} + \left(1 + \frac{\lambda}{k}\right) l} (ln\; r^* - l) \right] sin(2\pi t^*), \qquad (3.45)
$$

and

$$\begin{aligned} Q_s^* &= -\frac{\rho}{2\pi b_1 R^2} Q, \\ &= \frac{\rho R^2}{16\mu}\left\{(1-k^2)(1-k^2+4l) - \frac{1-k^2+2(1+k\lambda)l}{ln\frac{1}{k}+(1+\frac{\lambda}{k})l}[(1-k^2)(1+2l)+2k^2 ln(k)]\right\} \\ &\quad \times sin(2\pi t^*). \end{aligned} \tag{3.46}$$

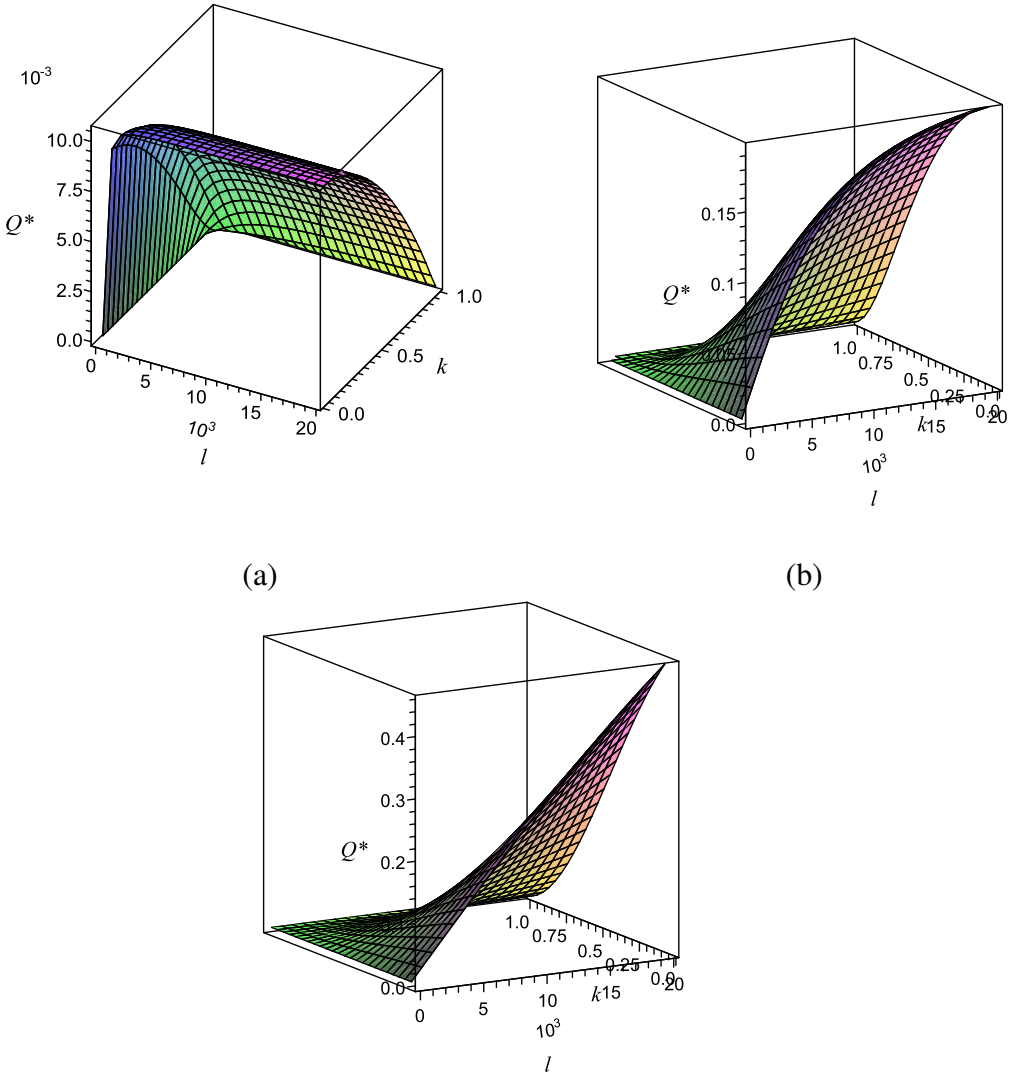

(a) (b)

(c)

Figure 3.3: Variation of the amplitude of the flow rate Q_m^* with l and k obtained for different frequencies $\omega = \alpha\mu/\rho R^2$ with (a) $\alpha = 0.005$, (b) $\alpha = 0.00025$, and (c) $\alpha = 0.00005$.

Figure 3.3 shows the variations of the amplitude of the flow rate with l and

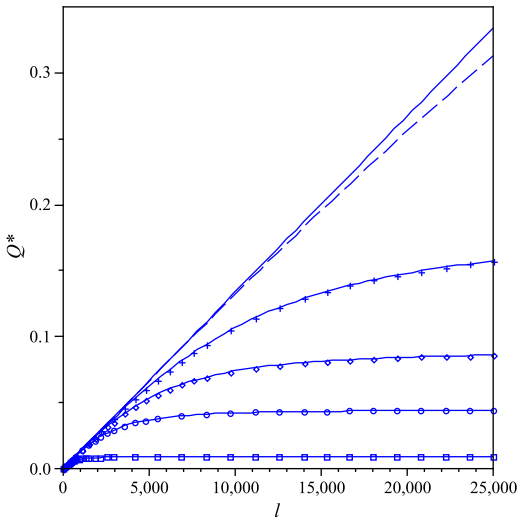

Figure 3.4: Influence of l on the quasi steady-state solution Q_s^* and the transient solution Q_m^* under different frequencies $\omega = \alpha\mu/\rho R^2$ with five different α values: $\alpha = 5.0 \times 10^{-3}$ (dash-box line), $\alpha = 1.0 \times 10^{-3}$ (dash-circle line), $\alpha = 5.0 \times 10^{-4}$ (dash-diamond line), $\alpha = 2.5 \times 10^{-4}$ (dash-cross line), $\alpha = 5.0 \times 10^{-5}$ (dash line).

k for different angular frequencies. Figure 3.4 shows the influence of l on Q_m^* for different angular frequency ω. Obviously, as the angular frequency decreases, the amplitude of the transient flow rate increases and the transient solution converges toward the quasi steady-state solution. It is also noted that the dependence of the amplitude of the transient flow rate on l is very different for different frequencies. At high frequency, the amplitude of the flow rate increases initially as l increases but tends to a constant value once l becomes sufficiently large. On the other hand, at low frequency the flow rate continues to increase with l and depends on l almost linearly for large l values.

Next, as an illustration, we investigate in more detail the influence of k and l on the flow rate for the frequency, $\omega = 5.0 \times 10^{-4}\mu/\rho R^2$, corresponding to a state that is not so close to the quasi steady state as shown by the dash-diamond line in Figure 3.4. We consider here the case where both the inner and outer surfaces have the same smoothness, i.e $\lambda = 1$. For this case, (3.44) give the amplitude of the normalized flow rate as a function of the variables l and k which is shown graphically in Figure 3.5. From the results, various findings can be obtained.

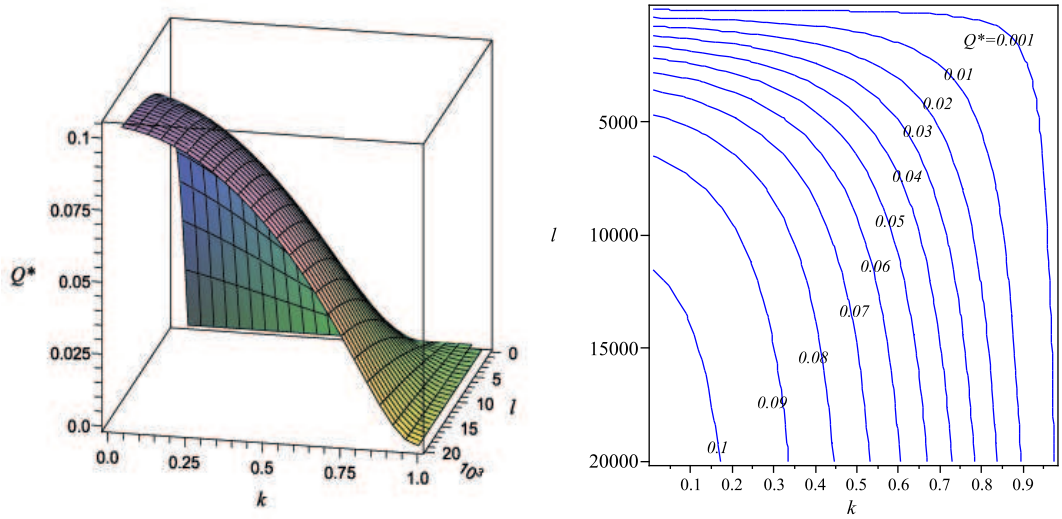

(a) (b)

Figure 3.5: Variation of the amplitude of the flow rate with l and k obtained from solution (44) with $\lambda = 1,\ R = 1.0 \times 10^{-5},\ \rho = 1060,\ \mu = 0.001,\ \omega = 5.0 \times 10^{-4}\ \mu/\rho R^2$: (a) 3D graph for Q_m^*; (b) contour plot of Q_m^* on (k, l) plane.

(i) Unlike for the case of constant pressure gradient, the flow rate in this case no longer increases linearly with l for large l values. For each fixed k value, as l increases, the flow rate increases first and then tends to a constant once l becomes large. The critical l value at which the amplitude of the flow rate tends to a constant value decreases with the increase of the k value.

(ii) The amplitude of the flow rate decreases as k increases, as shown in Figure 3.6. This is because the increase of k not only reduces the cross-section area for the fluid flow, but also leads to lower slip velocity on the solid surface as shown in Figure 3.7.

(iii) As for the constant case, one could have different (k, l) designs to achieve a given flow rate and Figure 3.5(b) provides a tool for the design.

(iv) The influence of l on the flow rate becomes less and less significant as k increases.

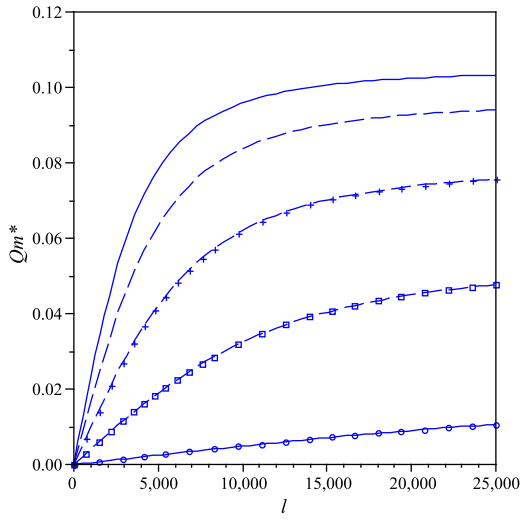

Figure 3.6: Variation of the amplitude of the flow rate with l for $\omega = 5.0 \times 10^{-4}\ \mu/\rho R^2$ and various different k values in case 2: $k = 0.1$ (solid line), $k = 0.3$ (dash line), $k = 0.5$ (dash-cross line), $k = 0.7$ (dash-box line), and $k = 0.9$ (solid-circle line).

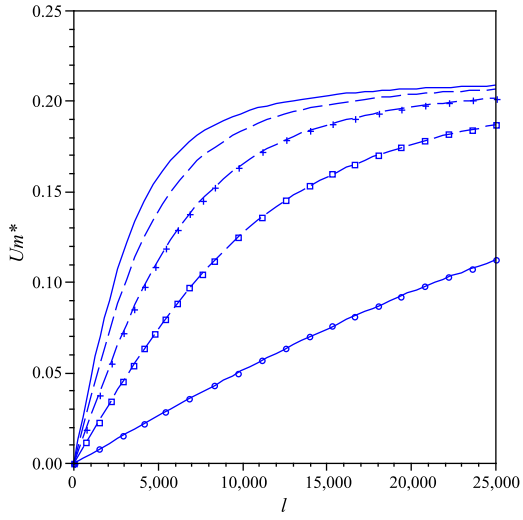

Figure 3.7: Variations of the amplitude of the slip velocity u_m^* on the outer surface $r^* = 1$ with l for $\omega = 5.0 \times 10^{-4}\ \mu/\rho R^2$ and various different k values in case 2: $k = 0.1$ (solid line), $k = 0.3$ (dash line), $k = 0.5$ (dash-cross line), $k = 0.7$ (dash-box line), and $k = 0.9$ (solid-circle line).

3.6 Concluding Remarks

In this section, we derive the exact solutions for the pressure gradient-driven transient flow of an incompressible Newtonian liquid through a circular annual with a Navier slip boundary. Based on the analytical expressions of the solutions, we analyze the influence of the slip parameter l and the geometry of the cross-section on the flow rate of fluid through the annual. The study shows that

(i) The influence of boundary slip on the flow through the annual is different for different types of pressure gradients. For flows driven by a constant pressure gradient, the flow rate always increases with the slip parameter l and achieves a linear increase rate for large l value; while, for the flows driven by the wave form pressure gradient with high frequency, the flow rate initially increases significantly as l increases from zero but tends to a constant when l becomes sufficiently large.

(ii) To achieve a fixed value of flow rate, one could have different (k, l) designs. The exact solutions obtained in this section, together with the contour plots of the solutions (Figure 3.2(b) and Figure 3.5(b)), provide a tool for engineers and scientists to determine the proper (k, l) values.

Chapter 4

Simulation of Particle-fluid Flow

4.1 General Overview

In this chapter, we present a mathematical model to describe the particle-fluid flow in micro-channels. The fluid is assumed to be Newtonian and the motion of particles is asumed to follow Newton's laws of motion. The finite element method, based on the Arbitary Lagrangian-Eulerian approach, is used to solve the problem. The stress and velocity fields in fluids and the particle movement are presented and discussed.

The rest of the chapter is organized as follows. The complete set of equations for the fluid-particle flow, based on the Newtonian model, is presented in section 4.2. In section 4.3, an Arbitary Lagrangian-Eulerian formulation for the mesh movement is presented. In section 4.4, a numerical scheme for solving the problem is developed based on the Bobnov-Galerkin finite element method and the Arbitary Lagrangian-Eulerian method. In section 4.5, the solution procedure for the problem is given. In section 4.6, a numerical investigation on the stress and velocity fields in fluids is presented followed by the numerical investigation on the movement of particles in section 4.7.

4.2 Formulation of the Problem

In this section, the mathematical model for the fluid flow and particle motion in fluids is described. The governing equations for the fluid flow include the Navier-Stokes equations and the continuity equation. The governing equations for particle

motion are Newton's second law of motion. The particle-particle interaction and particle-wall interaction are taken into account.

To study the motion of solid particles immersed in a fluid, we assume that the fluid-solid particle system occupies a bounded domain $\bar{\Omega}$ in $\mathbf{R}^3$. At a typical instant of time t, Q particles occupy Q closed connected subsets $\sum_{q=1}^{Q} \Omega_q \subset \mathbf{R}^3$ which are surrounded by a viscous homogeneous fluid filling the domain $\bar{\Omega} - \sum_{q=1}^{Q} \Omega_q$ called the flow-channel area.

In this study we use two coordinate systems: a reference system, Ω, where the model is drawn and the particle movement is solved, and a moving mesh system, Ω_{def}, corresponding to the deformed mesh of the flow channel, where we simulate the fluid flow. The time evolution of the domain Ω_{def} is determined by means of an Arbitrary Lagrangian-Eulerian (ALE) mapping $\mathbf{x} : \Omega \times \mathbf{R}^+ \mapsto \Omega_{def}$ which maps any point $(\mathbf{X}, t)$ in Ω to its image $\mathbf{x}(\mathbf{X}, t)$ in Ω_{def}.

Now we will formulate the mathematical model to describe the fluid flow and particle motion in fluids. Firstly, consider the model for fluid flow. Fluid is assumed to be an incompressible Newtonian fluid. The flow of fluid is described by the continuity equation and the Navier-Stokes equations, in terms of total derivatives,

$$\nabla \cdot \mathbf{u} = 0, \tag{4.1}$$

$$\rho_f \frac{D\mathbf{u}}{Dt} - \nabla \cdot \sigma = \mathbf{F}, \tag{4.2}$$

for $\mathbf{x} = (x, y, z)$ in $\Omega_{def}(t)$ where ρ_f denotes the blood density, $\mathbf{u} = [u_i]|_{i=1,2,3} = [u, v, w]^T$ represents the 3D velocity vector, and $\mathbf{F}$ is the volume force acting on the fluid. For this model, we neglect the effect of gravitational force and thus $\mathbf{F} = \mathbf{0}$. The quantity σ in equation (4.2) is the viscous stress tensor given by

$$\sigma = -p\mathbf{I} + \mu(\nabla\mathbf{u} + (\nabla\mathbf{u})^T), \tag{4.3}$$

where μ is the fluid viscosity, p is the fluid pressure, and δ_{ij} is the Kronecker symbol. The indicial expression of the equations (4.1)-(4.3) are

$$\frac{\partial u_j}{\partial x_j} = 0, \tag{4.4}$$

$$\rho_f \frac{Du_i}{Dt} - \frac{\partial \sigma_{ij}}{\partial x_j} = 0, \tag{4.5}$$

$$\sigma_{ij} = -p\delta_{ij} + \mu \left(\frac{\partial u_i}{\partial x_j} + \frac{\partial u_j}{\partial x_i} \right). \tag{4.6}$$

Two types of boundary conditions on the wall will be investigated in the work, incluiding the no-slip condition and the slip condition. Both types of boundary conditions can be written as

$$\mathbf{u} = -l \frac{\partial u}{\partial y} \text{ on } \Gamma_w, \tag{4.7}$$

where l is the slip parameter. It should be addressed here that $l = 0$ corresponds to the no-slip case.

The flow in microscale is known to be laminar profile. Thus the inlet boundary condition is assumed to be laminar, which is given by,

$$\begin{gathered} -L_{\text{enter}} \nabla_t \cdot (-p\mathbf{I} + \mu(\nabla_t \mathbf{u} + (\nabla_t \mathbf{u})^T) = -p_{\text{enter}} \mathbf{n} \text{ on } \Gamma_{\text{in}}, \\ \nabla_t \cdot \mathbf{u} = 0 \text{ on } \Gamma_{\text{in}}, \end{gathered} \tag{4.8}$$

where L_{enter} is the entrance length of the fictitious channel inlet, p_{enter} is the entrance pressure at the channel inlet, $\mathbf{n}$ is the outward normal vector. The pressure p_{enter} on the inlet is determined by solving (4.8) such that the computed average velocity of the laminar flow equals to a given mean velocity u_{mean}, and ∇_t denotes that this equation is solved for tangential components on the boundary.

On the outflow boundary Γ_{out}, the stress-free condition is used:

$$\sigma \cdot \mathbf{n} \ = \ 0 \quad \text{on } \Gamma_{\text{out}}. \tag{4.9}$$

On the boundary of particles, the velocity of blood is assumed to be the same as that of particles, which is

$$\mathbf{u} = \mathbf{V}_q \text{ on } \Gamma_q, \tag{4.10}$$

where $\mathbf{V}_q$ will be determined later.

Therefore the boundary conditions for the velocity field of fluids are of the

Dirichlet type and Neumann type,

$$\begin{aligned} -L_{\text{enter}}\nabla_t(-p\mathbf{I}+\mu(\nabla_t\mathbf{u}+(\nabla_t\mathbf{u})^T) &= -p_{\text{enter}}\mathbf{n} && \text{on } \Gamma_{\text{in}},\\ \nabla_t\cdot\mathbf{u} &= 0 && \text{on } \Gamma_{\text{in}},\\ u_t &= -l\frac{\partial u_t}{\partial y} && \text{on } \Gamma_w,\\ \mu(u_{i,j}+(u_{j,i}))\cdot\mathbf{n} &= 0 && \text{on } \Gamma_{\text{out}},\\ u_i &= V_{q_i} && \text{on } \Gamma_q. \end{aligned} \tag{4.11}$$

Now consider the mathematical model for particle flow. To study the motion of particles in the fluid flow channel, we assume that the gravitational force can be neglected and the particle motion is governed by Newton's second law:

$$\begin{aligned} &m_q\tfrac{\partial\mathbf{V}_q}{\partial t}=\mathbf{F}_v+\mathbf{F}_q, \quad q=1,2,3...,Q\\ &\mathbf{V}_q|_{t=0} = 0. \end{aligned} \tag{4.12}$$

The position $\mathbf{X}_q$ of the center of the qth particle can be determined by the equation:

$$\begin{aligned} \tfrac{d\mathbf{X}_q}{dt} &= \mathbf{V}_q\ , \qquad q=1,2,3...,Q\\ \mathbf{X}_q|_{t=0} &= \mathbf{X}_q^0. \end{aligned} \tag{4.13}$$

In equation $(4.12)_1$, $\mathbf{V}_q$ and m_q denote, respectively, the velocity vector and the mass of the qth particle. Next, we will determine the two applied loads, drag force $\mathbf{F}_v$ and collision force $\mathbf{F}_q$. For the drag force $\mathbf{F}_v$ acting on particle Ω_q, it is assumed that all the boundaries of particles experience drag force $\mathbf{F}_v$ from the fluid given by

$$\mathbf{F}_v=\int_{\partial\Omega_q}(-\mathbf{n}_f\cdot\sigma)dS=-\int_{\partial\Omega_q}\mathbf{n}_f\cdot(-p\,\mathbf{I}+\eta(\nabla\mathbf{u}+(\nabla\mathbf{u})^T))dS, \tag{4.14}$$

where $\mathbf{n}_f$ is the normal vector of the fluid domain. It is seen that the drag force $\mathbf{F}_v$ consists of the pressure and the viscous drag of the fluid. To prevent collision among the particles and the collision between the particles and vessel walls, the particle-particle interaction force $\mathbf{F}_{q,p}$ and the particle-wall interaction force $\mathbf{F}_{q,w}$ are applied when the distance between two particles, or between a particle and a wall, is within the order of the element size [70]. Thus

$$\mathbf{F}_q=\sum_{p=1,p\neq q}^{Q}\mathbf{F}_{q,p}+\sum_{w=1}^{2}\mathbf{F}_{q,w}, \tag{4.15}$$

in which

$$\mathbf{F}_{q,p} = \begin{cases} 0, \text{ for } d_{q,p} > R_q + R_p + \alpha \\ \frac{1}{\varepsilon_q}(\mathbf{X}_q - \mathbf{X}_p)(R_q + R_p + \alpha - d_{q,p})^2, \text{ for } d_{q,p} \leq R_q + R_p + \alpha \end{cases} \tag{4.16}$$

and

$$\mathbf{F}_{q,w} = \begin{cases} 0, \text{ for } d_{q,w} > 2R_q + \alpha \\ \frac{1}{\varepsilon_w}(\mathbf{X}_q - \mathbf{X}_w)(2R_q + \alpha - d_{q,w})^2, \text{ for } d_{q,w} \leq 2R_q + \alpha \end{cases} \tag{4.17}$$

where $d_{q,p}$ denotes the distance between the centers of the qth and pth particles, $d_{q,w}$ denotes the distance between the centers of the qth particle and the imaginary particle on the other side of the wall, $\mathbf{X}_q$ and R_q are respectively the center and radius of the qth particle, α is the force range, and ε_q and ε_w are small positive stiffness parameters.

4.3 Arbitary Lagrangian-Eulerian (ALE) Mesh Movement

In order to construct a mesh-based numerical model involving the motion of particles in fluids, we will introduce the Arbitary Lagrangian-Eulerian method which will involve the mesh movement of the numerical model.

We follow the ALE description given by [96]. The method is restated as follow. Let ϕ be a scalar variable of x in $\Omega_{def}(t)$ and t. The variable ϕ is transported from a position P at a time t to a new position P_f at $t + \triangle t$ with a velocity of $\mathbf{u}$. The mesh point is moved to a new position P_r at $t + \triangle t$ with a mesh velocity of $\mathbf{\Psi}$. Using Taylor series expansion in time, we calculate ϕ for position P_f at time $t + \triangle t$ by

$$\phi_{P_f}^{n+1} = \phi_{P_f}^{n} + \triangle t \frac{\partial \phi_{P_f}^{n}}{\partial t} + \dots \ . \tag{4.18}$$

Using Taylor series expansion in space, we express ϕ for position P_f at time t by

$$\phi_{P_f}^{n} = \phi_{P}^{n} + u_i \triangle t \frac{\partial \phi_{P}^{n}}{\partial x_i} + \dots, \tag{4.19}$$

where $x_i = x, y, z$ for $i = 1, 2, 3$, respectively.

Substituting (4.21) into (4.18), we have

$$\begin{aligned}\phi_{P_f} = \phi^{n+1} &= \phi_P^n + u_i \triangle t \frac{\partial \phi_P^n}{\partial x_i} + \triangle t \frac{\partial}{\partial t}\left(\phi_P^n + u_i \triangle t \frac{\partial \phi_P^n}{\partial x_i}\right) + \ldots, \\ &= \phi_P^n + \triangle t \frac{\partial \phi_P^n}{\partial t} + u_i \triangle t \frac{\partial \phi_P^n}{\partial x_i} + \ldots \ .\end{aligned} \tag{4.20}$$

Similarly, we express ϕ at position P_r at time t, using Taylor series expansion in time, as

$$\phi_{P_r} = \phi^n = \phi_P^n + \Psi_i \triangle t \frac{\partial \phi_P^n}{\partial x_i} + \ldots, \tag{4.21}$$

where $\Psi_i = \Psi_x, \Psi_y, \Psi_z$ for $i = 1, 2, 3$, respectively.

Neglecting second and higher order terms, the relative value of ϕ between the actual particle and the mesh motion is then given by

$$\triangle \phi = \phi^{n+1} - \phi^n = \triangle t \frac{\partial \phi_P^n}{\partial t} + (u_i - \Psi_i) \triangle t \frac{\partial \phi_P^n}{\partial x_i}. \tag{4.22}$$

As $\triangle t \to 0$ and dropping super and subscripts, (4.22) can be rewritten as

$$\frac{D\phi}{Dt} = \frac{\partial \phi}{\partial t} + (u_i - \Psi_i) c, \tag{4.23}$$

or

$$\frac{D\phi}{Dt} = \frac{\partial \phi}{\partial t} + (\mathbf{u} - \mathbf{\Psi}) \cdot \nabla \phi. \tag{4.24}$$

These total derivatives in the ALE form will be used to describe the motion of material in the ALE frame.

In the ALE coordinate system, the continuity equation (4.1) and the Navier-Stokes equations (4.2) can be, using the total derivatives in the ALE form (4.24), written as,

$$\frac{\partial u_i}{\partial x_i} = 0, \tag{4.25}$$

$$\rho_f \frac{\partial u_i}{\partial t} + \rho_f (u_j - \Psi_j) \frac{\partial u_i}{\partial x_j} - \frac{\partial \sigma_{ij}}{\partial x_j} = 0. \tag{4.26}$$

Due to the movement of the coordinate system, the mesh velocity $\mathbf{\Psi} = (\Psi_x, \Psi_y, \Psi_z)$ is introduced in the deformed domain Ω_{def}. To guarantee a smoothly varying distribution of the nodes, we assume that the nodes on $\partial\Omega_q$ move with the particle (no slip) and that each component of the mesh velocity in the fluid channel is governed by a Laplace equation:

$$\nabla^2 \mathbf{\Psi} = \mathbf{0}, \quad \forall \mathbf{x} \in \Omega_{def}. \tag{4.27}$$

The above equation is to smooth gradient of the mesh velocity over the domain so as to reduce mesh distortion. Once the mesh velocity components are determined, we can determine the smoothed deformed mesh for the flow channel at each time instant by updating the coordinates of the nodes according to the following formulae

$$\begin{array}{rcl} x & = & X + \int_0^t \Psi_x \, dt, \\ y & = & Y + \int_0^t \Psi_y \, dt, \\ z & = & Z + \int_0^t \Psi_z \, dt. \end{array} \tag{4.28}$$

Another condition that needs to be specified is that the fluid, particle and mesh all move with the same velocity on the particle boundaries, i.e.,

$$\mathbf{\Psi} \; = \; \mathbf{u} \; = \; \mathbf{V}_q \quad \text{on} \;\; \partial\Omega_q. \tag{4.29}$$

4.4 Finite Element Formulation

In order to study the flow of particles, we implement the finite element approach based on the Arbitary Lagrangian-Eulerian method.

Substituting the stress tensor term from equation (4.6) into equation (4.26), we obtain the following Navier–Stokes equations

$$\rho_f \left(\frac{\partial u_i}{\partial t} + (u_j - \Psi_j) u_{i,j} \right) - \left(\mu (u_{i,j} + u_{j,i}) \right)_{,j} + p_{,i} \; = \; 0. \tag{4.30}$$

Note that a new variable Ψ_j of mesh velocity is added to the Navier–Stokes equations.

It is seen that these Navier–Stokes equations together with the continuity equation (4.25) constitute a closed system of seven partial differential equations in terms of seven coordinate and time–dependent unknown functions u_1, u_2, u_3, p, Ψ_1 Ψ_2, and Ψ_3.

Now we have a complete set of equations to describe the fluid flow and particle flow in fluid. The governing equations consist of the continuity equation (4.25), the Navier-Stokes equations (4.30), and the Laplace equation for mesh smoothing (4.27). For convenience in formulation, we rewrite equations (4.27) in the indicial notation as follows,

$$\Psi_{i,jj} = 0. \tag{4.31}$$

The field equations (4.25), (4.30), and (4.31) are defined in $\Omega_{def}(t)$ with the boundary conditions (4.11) and (4.29). These equations and boundary conditions constitute a closed system of seven partial differential equations in terms of seven unknown functions u_i, p, Ψ_i. The system, supplemented by the initial condition and the boundary conditions (4.11) and (4.29), can be solved numerically to yield the velocity field and the pressure distribution and consequently the shear stresses on the wall. Thus, the boundary value problem for the fluid-particle flow problem is as follows:

BVP: Find u_i, p, Ψ_i such that the field equations (4.25), (4.30), and (4.31) are satisfied in $\Omega_{def}(t)$ and all boundary conditions (4.11) and (4.29) are satisfied.

To derive a variational statement for the BVP, we consider the following associated variational boundary value problem.

VBVP: Find $u_i, p, \Psi_i \in \mathrm{H}^1(\Omega_{def})$ in the deformed mesh system at each time instant such that all the Dirichlet boundary conditions (4.11) and (4.29) are satisfied and for all $\hat{u}_i \in \mathrm{H}^1_{u_i}(\Omega_{def}) \equiv \{\hat{u}_i \in \mathrm{H}^1(\Omega_{def}) | \hat{u}_i = 0 \text{ on } \partial\Omega_{def_{u_i}}\}$, $\hat{p} \in \mathrm{H}^1_p(\Omega_{def}) \equiv \{\hat{p} \in \mathrm{H}^1(\Omega_{def}) | \hat{p} = 0 \text{ on } \partial\Omega_{def_p}\}$, $\hat{\Psi}_i \in \mathrm{H}^1_{\Psi_i}(\Omega_{def}) \equiv \{\hat{\Psi}_i \in \mathrm{H}^1(\Omega_{def}) | \hat{\Psi}_i = 0 \text{ on } \partial\Omega_{def_{\Psi_i}}\}$, and

$$(u_{i,i}, \hat{p}) = 0, \tag{4.32}$$

$$\left(\rho_f \frac{\partial u_i}{\partial t}, \hat{u}_i\right) + \left(\rho_f (u_j - \Psi_j) u_{i,j}, \hat{u}_i\right) - \left(\mu (u_{i,j} + u_{j,i})_{,j}, \hat{u}_i\right) + \left(p_{,i}, \hat{u}_i\right) = 0, \tag{4.33}$$

and

$$(\Psi_{i,jj}, \hat{\Psi}_i) = 0, \tag{4.34}$$

where $\partial\Omega_{def_{\mathbf{u_i}}}$, $\partial\Omega_{def_p}$, and $\partial\Omega_{def_{\mathbf{\Psi_i}}}$ are the parts of boundary where the velocity, the pressure, and the mesh velocity are specified. $\mathrm{H}^1(\Omega_{def})$ is the Sobolev space $W^{1,2}(\Omega_{def})$ with norm $\|\cdot\|_{1,2,\Omega_{def}}$ and the inner product $(\cdot,\cdot)$ is defined by

$$(a, b) = \int_{\Omega_{def}} (ab) d\Omega. \tag{4.35}$$

Using the continuity equation, the integration by parts technique, the divergence theorem, and the boundary condition, we can eliminate the second order derivatives in (4.33) and (4.34) to obtain

$$\Big(\rho_f \frac{\partial u_i}{\partial t}, \hat{u}_i\Big) + \Big(\rho_f (u_j - \Psi_j) u_{i,j}, \hat{u}_i\Big) + \mu\Big(u_{i,j}, \hat{u}_{i,j}\Big) + \Big(p_{,i}, \hat{u}_i\Big) - \mu\Big(u_{i,j} n_j, \hat{u}_i\Big)_B = 0, \tag{4.36}$$

and

$$(\Psi_{i,j}, \hat{\Psi}_{i,j}) = 0, \tag{4.37}$$

where $(a, b)_B$ denotes integration of ab over the boundary of Ω except for the part with Dirichlet boundary condition.

Since the computations are conducted in the reference coordinates, Ω, we need to transform equations (4.32), (4.36), and (4.37) in the deformed coordinates to those equations in the reference coordinates. Through this, the inner product expression in (4.35) is re-defined as

$$(a, b) = \int_{\Omega_{def}} (ab) d\Omega = \int_{\Omega} (ab)\ |\mathbf{J}|\ d\Omega, \tag{4.38}$$

where the so-called Jacobian matrix **J** and the derivatives of the unknown functions u_i, p and Ψ_i in equations (4.32), (4.36), and (4.37) are defined as follows.

In the flow-channel area, the two coordinate systems, $(X, Y, Z) \in \Omega$ and $(x, y, z) \in \Omega_{def}$, are connected through a transformation T. At the initial state at $t = 0$, the two mesh systems are assumed to coincide. The transformation T maps the point initially located at (X, Y, Z) to the point (x, y, z) at time t:

$$T : \begin{aligned} x &= x(X, Y, Z, t) \\ y &= y(X, Y, Z, t) \\ z &= z(X, Y, Z, t). \end{aligned}$$

Suppose that the functions $x,\ y$ and z are continuous differentiable with respect to $X,\ Y,\ Z$. Then the infinitesimals $dX,\ dY,\ dZ$ transform into $dx,\ dy,\ dz$ according to

$$\begin{aligned} dx &= x_{,X} dX + x_{,Y} dY + x_{,Z} dZ, \\ dy &= y_{,X} dX + y_{,Y} dY + y_{,Z} dZ, \\ dz &= z_{,X} dX + z_{,Y} dY + z_{,Z} dZ, \end{aligned} \tag{4.39}$$

where $(\cdot)_{,X}$ denotes differentiation with respect to X. System (4.39) can be written in matrix form as

$$\begin{bmatrix} dx \\ dy \\ dz \end{bmatrix} = \begin{bmatrix} x_{,X} & x_{,Y} & x_{,Z} \\ y_{,X} & y_{,Y} & y_{,Z} \\ z_{,X} & z_{,Y} & z_{,Z} \end{bmatrix} \begin{bmatrix} dX \\ dY \\ dZ \end{bmatrix}. \tag{4.40}$$

The 3×3 matrix of partial derivatives in (4.40) is called the Jacobian matrix of the transformation. Denote the matrix by $\mathbf{J}$, then

$$|\mathbf{J}| = x_{,X}(y_{,Y}z_{,Z} - y_{,Z}z_{,Y}) - x_{,Y}(y_{,X}z_{,Z} - y_{,Z}z_{,X}) + x_{,Z}(y_{,X}z_{,Y} - y_{,Y}z_{,X}).$$

For $|\mathbf{J}| \neq 0$, the transformation is invertible and there exists an inverse transformation at time t, i.e.,

$$T^{-1} : \begin{aligned} X &= X(x, y, z) \\ Y &= Y(x, y, z) \\ Z &= Z(x, y, z). \end{aligned}$$

As in (4.40), we have

$$\begin{bmatrix} dX \\ dY \\ dZ \end{bmatrix} = \begin{bmatrix} X_{,x} & X_{,y} & X_{,z} \\ Y_{,x} & Y_{,y} & Y_{,z} \\ Z_{,x} & Z_{,y} & Z_{,z} \end{bmatrix} \begin{bmatrix} dx \\ dy \\ dz \end{bmatrix}. \tag{4.41}$$

From (4.40), we also have

$$\begin{bmatrix} dX \\ dY \\ dZ \end{bmatrix} = \mathbf{J}^{-1} \begin{bmatrix} dx \\ dy \\ dz \end{bmatrix}, \tag{4.42}$$

where

$$\mathbf{J}^{-1} = \frac{1}{|\mathbf{J}|} \begin{bmatrix} y_{,Y}z_{,Z} - y_{,Z}z_{,Y} & x_{,Z}z_{,Y} - x_{,Y}z_{,Z} & x_{,Y}y_{,Z} - x_{,Z}y_{,Y} \\ y_{,Z}z_{,X} - y_{,X}z_{,Z} & x_{,X}z_{,Z} - x_{,Z}z_{,X} & y_{,X}x_{,Z} - y_{,Z}x_{,X} \\ y_{,X}z_{,Y} - y_{,Y}z_{,X} & x_{,Y}z_{,X} - x_{,X}z_{,Y} & x_{,X}y_{,Y} - x_{,Y}y_{,X} \end{bmatrix}, \tag{4.43}$$

Equating terms in (4.41) and (4.42), we obtain

$$\begin{aligned}
X_{,x} &= \tfrac{1}{|\mathbf{J}|}(y_{,Y}z_{,Z} - y_{,Z}z_{,Y}),\\
X_{,y} &= \tfrac{1}{|\mathbf{J}|}(x_{,Z}z_{,Y} - x_{,Y}z_{,Z}),\\
X_{,z} &= \tfrac{1}{|\mathbf{J}|}(x_{,Y}y_{,Z} - x_{,Z}y_{,Y}),\\
Y_{,x} &= \tfrac{1}{|\mathbf{J}|}(y_{,Z}z_{,X} - y_{,X}z_{,Z}),\\
Y_{,y} &= \tfrac{1}{|\mathbf{J}|}(x_{,X}z_{,Z} - x_{,Z}z_{,X}),\\
Y_{,z} &= \tfrac{1}{|\mathbf{J}|}(y_{,X}x_{,Z} - y_{,Z}x_{,X}),\\
Z_{,x} &= \tfrac{1}{|\mathbf{J}|}(y_{,X}z_{,Y} - y_{,Y}z_{,X}),\\
Z_{,y} &= \tfrac{1}{|\mathbf{J}|}(x_{,Y}z_{,X} - x_{,X}z_{,Y}),\\
Z_{,z} &= \tfrac{1}{|\mathbf{J}|}(x_{,X}y_{,Y} - x_{,Y}y_{,X}).
\end{aligned} \tag{4.44}$$

These relations are crucial in transforming the calculation results from Ω_{def} to Ω.

Now the derivatives of the unknown functions φ_i $(i = x, y, z)$, where φ_i represents u_i, p, and Ψ_i, can be determined by the following expressions:

$$\begin{aligned}
\varphi_{i,x} &= \varphi_{i,X}X_{,x} + \varphi_{i,Y}Y_{,x} + \varphi_{i,Z}Z_{,x},\\
\varphi_{i,y} &= \varphi_{i,X}X_{,y} + \varphi_{i,Y}Y_{,y} + \varphi_{i,Z}Z_{,y},\\
\varphi_{i,z} &= \varphi_{i,X}X_{,z} + \varphi_{i,Y}Y_{,z} + \varphi_{i,Z}Z_{,z},
\end{aligned} \tag{4.45}$$

or

$$\varphi_{i,j} = \varphi_{i,X_k}X_{k,j}, \tag{4.46}$$

and for the test functions:

$$\begin{aligned}
\hat{\varphi}_{i,x} &= \hat{\varphi}_{i,X}X_{,x} + \hat{\varphi}_{i,Y}Y_{,x} + \hat{\varphi}_{i,Z}Z_{,x},\\
\hat{\varphi}_{i,y} &= \hat{\varphi}_{i,X}X_{,y} + \hat{\varphi}_{i,Y}Y_{,y} + \hat{\varphi}_{i,Z}Z_{,y},\\
\hat{\varphi}_{i,z} &= \hat{\varphi}_{i,X}X_{,z} + \hat{\varphi}_{i,Y}Y_{,z} + \hat{\varphi}_{i,Z}Z_{,z},
\end{aligned} \tag{4.47}$$

or

$$\hat{\varphi}_{i,j} = \hat{\varphi}_{i,X_k}X_{k,j}. \tag{4.48}$$

Using (4.46) and (4.48), equations (4.32)-(4.34) become

$$(u_{i,X_k}X_{k,i}, \hat{p}) = 0, \tag{4.49}$$

$$\begin{aligned}
&\Big(\rho_f\frac{\partial u_i}{\partial t}, \hat{u}_i\Big) + \Big(\rho_f(u_j - \Psi_j)u_{i,X_k}X_{k,j}, \hat{u}_i\Big)\\
+\mu\Big(u_{i,X_k}X_{k,j}, \hat{u}_{i,X_k}X_{k,j}\Big) &+ \Big(p_{,X_k}X_{k,i}, \hat{u}_i\Big) - \mu\Big(u_{i,X_k}X_{k,j}, \hat{u}_i\Big)_B = 0,
\end{aligned} \tag{4.50}$$

$$\left(\Psi_{i,X_k} X_{k,j}, \hat{\Psi}_{i,X_k} X_{k,j}\right) = 0. \tag{4.51}$$

To get the solution of the above VBVP problem, the Bubnov-Galerkin finite element method is used in this work. We choose an M-dimensional subspace $H_h \subset H^1(\Omega_{def})$ for u_i, Ψ_i and the corresponding test functions, and N-dimensional subspace for $H_\beta \subset H^1(\Omega_{def})$ for p and the corresponding test functions. Let $\{\phi_m\}_{m=1}^M$ be the basis functions of H_h, and $\{\phi_n^p\}_{n=1}^N$ be the basis functions of H_β. Then we have

$$u_i(\mathbf{X}, t) \approx (u_i)_h = \sum_{m=1}^{M} \phi_m(\mathbf{X})(u_i)_m(t). \tag{4.52}$$

$$\hat{u}_i(\mathbf{X}, t) \approx (\hat{u}_i)_h = \sum_{m=1}^{M} \phi_m(\mathbf{X})(\hat{u}_i)_m(t). \tag{4.53}$$

$$\Psi_i(\mathbf{X}, t) \approx (\Psi_i)_h = \sum_{m=1}^{M} \phi_m(\mathbf{X})(\Psi_i)_m(t). \tag{4.54}$$

$$\hat{\Psi}_i(\mathbf{X}, t) \approx (\hat{\Psi}_i)_h = \sum_{m=1}^{M} \phi_m(\mathbf{X})(\hat{\Psi}_i)_m(t). \tag{4.55}$$

$$p(\mathbf{X}, t) \approx p_h = \sum_{n=1}^{N} \phi_n^p(\mathbf{X}) p_n(t). \tag{4.56}$$

$$\hat{p}(\mathbf{X}, t) \approx \hat{p}_h = \sum_{n=1}^{N} \phi_n^p(\mathbf{X}) \hat{p}_n(t). \tag{4.57}$$

Substituting equations (4.52)-(4.57) into equations (4.49)-(4.51) and using the arbitrary of $(\hat{u}_i)_m$, $(\hat{\Psi}_i)_m$, and $\hat{p}_n$, we obtain the following system of equations

$$\sum_{m=1}^{M} \int_\Omega \phi_q^p \frac{\partial \phi_m}{\partial X_k} \frac{\partial X_k}{\partial x_i} |\mathbf{J}| d\Omega (\mathbf{U}_i)_m = 0, \tag{4.58}$$

$$\rho_f \sum_{m=1}^{M} \int_{\Omega} \phi_k \phi_m |\mathbf{J}| d\Omega (\dot{\mathbf{U}}_i)_m$$

$$+\rho_f \sum_{m=1}^{M} \int_{\Omega} \phi_k (u_j - \Psi_j) \frac{\partial \phi_m}{\partial X_p} \frac{\partial X_p}{\partial x_j} |\mathbf{J}| d\Omega (\mathbf{U}_i)_m$$

$$+ \sum_{m=1}^{M} \int_{\Omega} \mu \frac{\partial \phi_k}{\partial X_l} \frac{\partial X_l}{\partial x_j} \frac{\partial \phi_m}{\partial X_p} \frac{\partial X_p}{\partial x_j} |\mathbf{J}| d\Omega (\mathbf{U}_i)_m \tag{4.59}$$

$$+ \sum_{n=1}^{N} \int_{\Omega} \phi_k \frac{\partial \phi_n^p}{\partial X_k} \frac{\partial X_k}{\partial x_i} |\mathbf{J}| d\Omega (\mathbf{P})_n$$

$$- \sum_{m=1}^{M} \int_{\partial\Omega} \phi_k \frac{\partial \phi_m}{\partial X_l} \frac{\partial X_l}{\partial x_j} |\mathbf{J}| dS (\mathbf{U}_i)_m = 0,$$

$$\sum_{m=1}^{M} \int_{\Omega} \frac{\partial \phi_k}{\partial X_l} \frac{\partial X_l}{\partial x_j} \frac{\partial \phi_m}{\partial X_p} \frac{\partial X_p}{\partial x_j} |\mathbf{J}| d\Omega (\mathbf{\Psi}_i)_m = 0. \tag{4.60}$$

We then apply boundary conditions (4.11) and (4.29) to equations (4.58)-(4.60). After a mathematical derivation, we obtain a system of ordinary differential equations which can be written in the terms of global vectors of $\mathbf{u}, p$, and $\mathbf{\Psi}$ with each ith entry representing the value of the corresponding unknown function at the ith node of the finite element mesh.

A standard backward Euler scheme is then used to solve the system of ordinary differential equations to determine the velocity and pressure fields at any instant of time.

4.5 Solution Procedure

Based on the previous formulation, the solution procedure for solving the fluid flow-particle motion problem is summarized as follows.

Initialization: $t_0 = 0, n = 0$ (index for time step),

Generate initial mesh $\mathbf{x}_0$ based on particle positions, $\mathbf{X}_q^i(0)$.

Initialize $\mathbf{u}(\mathbf{X}, t_0)$.

Do $n = 1, 2, \ldots, N$ (total number of time steps)

1. Select time step $\triangle t_n : t_n = t_{n-1} + \triangle t_n$.

2. Update particle positions:

   $\mathbf{X}_q^i(t_n) = \mathbf{X}_q^i(t_{n-1}) + \mathbf{V}_q^i(t_{n-1})\triangle t_n.$

3. Update mesh nodes:

   $\mathbf{y}(t_n) = \mathbf{x}(\mathbf{X}, t_{n-1}) + \mathbf{\Psi}(\mathbf{X}, t_{n-1})\triangle t_n.$

4. Check mesh quality; if the updated mesh $\mathbf{y}(t_n)$ is not too deformed, then generate a new mesh $\mathbf{x}(t_n)$, and then project the flow field from $\mathbf{y}(t_n)$ onto $\mathbf{x}(t_n)$.

5. Iteratively solve for the flow field $\mathbf{u}(\mathbf{x}(t_n), t_n)$, and $p(\mathbf{x}(t_n), t_n)$; the mesh velocity $\mathbf{\Psi}(\mathbf{x}(t_n), t_n)$; and the particle velocities $\mathbf{V}_q^i(t_n)$.

6. Update $\dot{\mathbf{V}}_q^i(t_n)$ from the equation (4.13).

7. Solve the mesh acceleration.

End Do.

4.6 Stress and Velocity Fields in Fluids

We consider here an example to study the flow of a Newtonian fluid passing around a solid cylinder in a microchannel with slip boundary. The cylinder is located at a fixed position in the middle of the channel. The height of the microchannel is $1.2\mu\,\mathrm{m}$, and the length $3\mu\,\mathrm{m}$, while the radius of the cylinder is $0.1\mu\,\mathrm{m}$. Other parameters have the values as follows: fluid density $\rho_f = 1000\,\mathrm{kg}\,/\,\mathrm{m}^3$, viscosity of fluid is $\mu = 0.001\,\mathrm{kg}\,/(\mathrm{m}\cdot\mathrm{s})$, slip parameters $l = 0$ (no slip), $0.25 \times 10^{-7}, 0.5 \times 10^{-7}, 1.0 \times 10^{-7}$, and 2.0×10^{-7}.

The finite element method presented in the previous sections is used to simulate the fluid flow through the microchannel at the presence of a particle on the channel. The aim is to investigate the influence of the slip parameter on the flow behaviour. Figure 4.1 shows the computational domain and its finite element mesh consisting of 27439 elements together with the coordinates used.

Figure 4.2 (a–c) shows the profiles of the velocity u_x on the channel cross-section at three different locations along the channel for five different values of the slip parameter l. The results show that at the upstream and downstream sufficiently

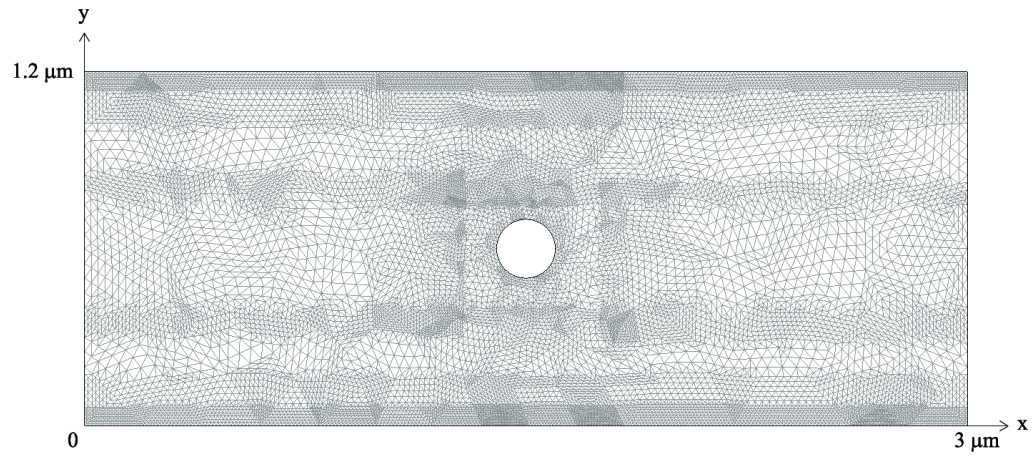

Figure 4.1: The computation domain and its finite element mesh together with the coordinates.

far from the cylinder, the velocity profile is parabolic for $l = 0$ (no slip) and tends to uniform as l increases. It can also be noted that the velocity increases significantly as the slip parameter l increases.

Figure 4.3 shows the the influence of the slip parameter l on the drag force exerted on the microcylinder surface by the fluid. It is clear from the results that as l increases, the drag force increases significantly.

Figure 4.4 shows the flow rate of fluid calculated at the outlet end of the microchannel for five different values of slip parameter $l = 0$ (or no slip), 0.25×10^{-7}, 0.5×10^{-7}, 1.0×10^{-7}, and 2.0×10^{-7}. The results show that the slip parameter has significantly influences on the flow rate. As l increases, the flow rate increases.

Figure 4.5 depicts the steamlines and velocity field of flow in the micro channel for five different values of slip parameter $l = 0$ (no slip), 0.25×10^{-7}, 0.5×10^{-7}, 1.0×10^{-7}, and 2.0×10^{-7}. The plots shows the pattern of fluid flow. In downstream from the cylinder, the velocity profile is similar to that in upstream. As l increases, the fluid flows faster in the region near the microchannel wall than in the region near the surface of the cylinder.

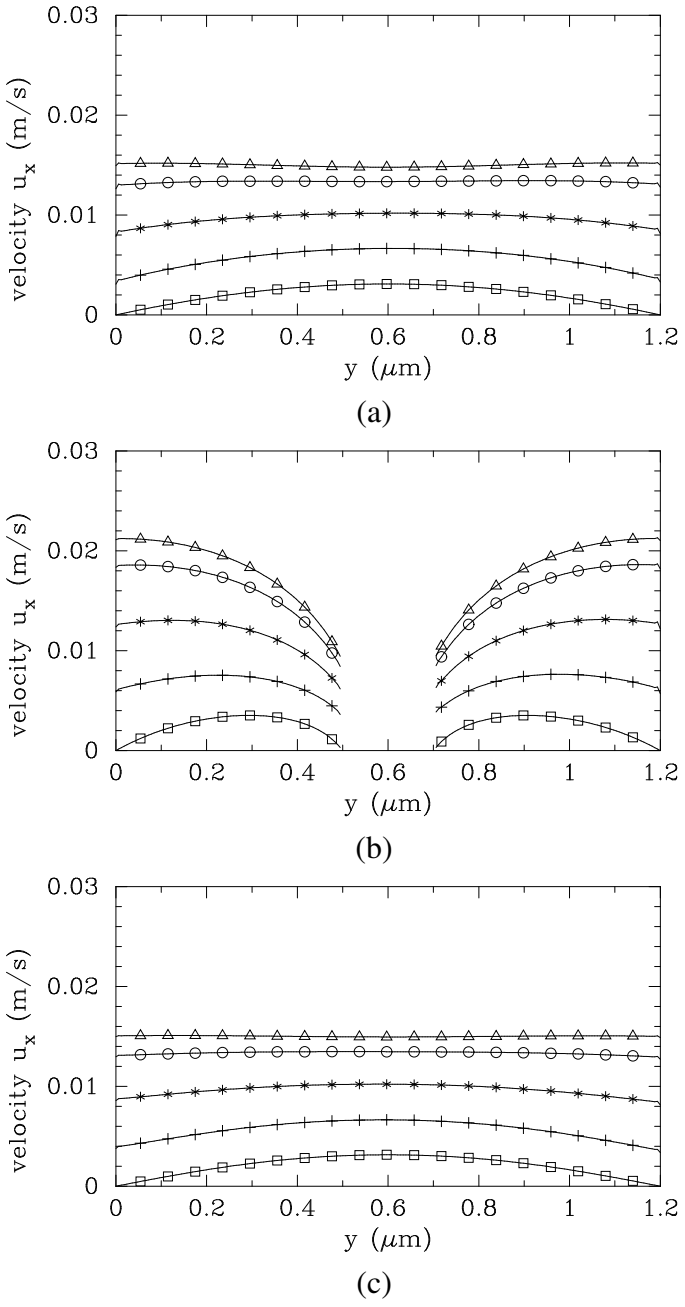

Figure 4.2: Cross-section profile of the velocity u_x at three different locations along the channel for five different slip parameter values $l = 0$ (or no slip) (solid-box line), $l = 0.25 \times 10^{-7}$ (solid-cross line), $l = 0.5 \times 10^{-7}$ (solid-asterisk line), $l = 1.0 \times 10^{-7}$ (solid-circle line), and $l = 2.0 \times 10^{-7}$ (solid-triangle line): (a) at the location $x = 0.5\mu\,\mathrm{m}$, (b) at the location $x = 1.5\mu\,\mathrm{m}$ (through the center of the microcylinder), and (c) at the location $x = 2.5\mu\,\mathrm{m}$ along the microchannel. The x and y coordinates are shown in Figure 4.1.

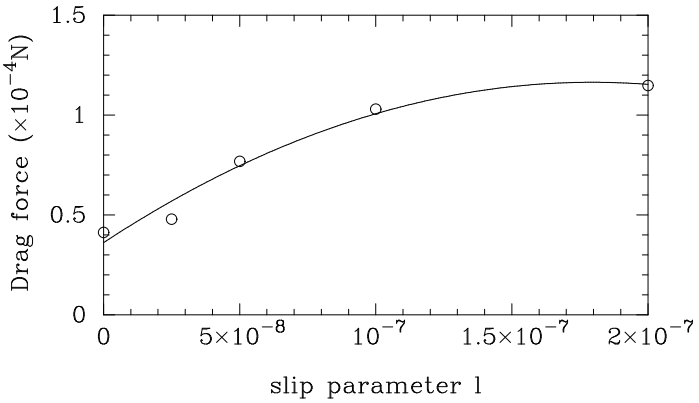

Figure 4.3: Influence of the slip parameter l on the drag force exerted on the cylinder by fluid. The circles represent numerical results, while the solid line is the least square fitting of the numerical results.

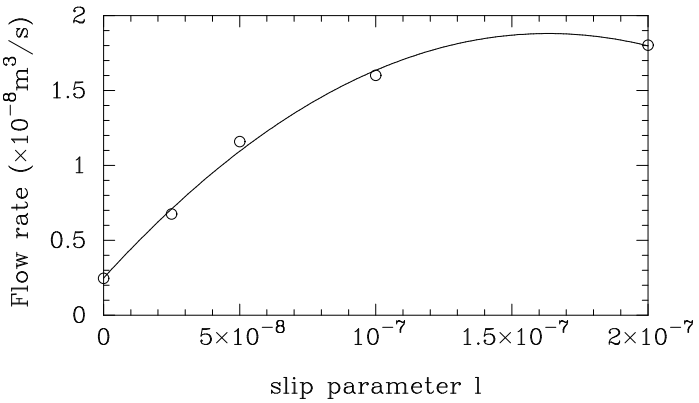

Figure 4.4: Influence of the slip parameter l on the flow rate of fluid through the microchannel.

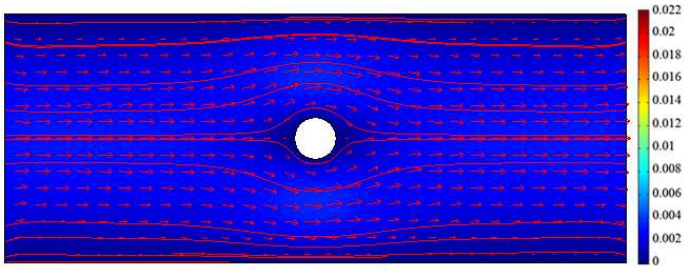

(a)

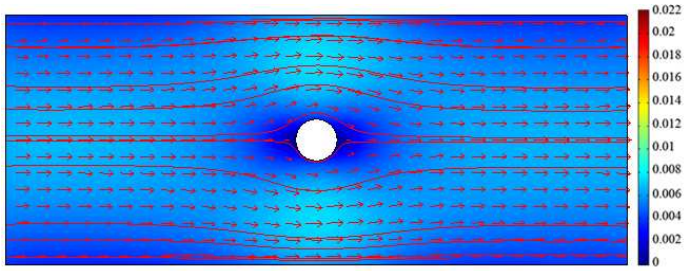

(b)

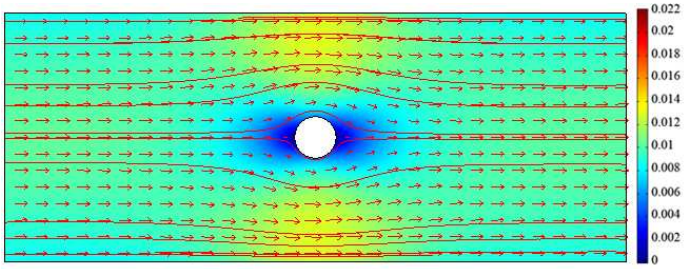

(c)

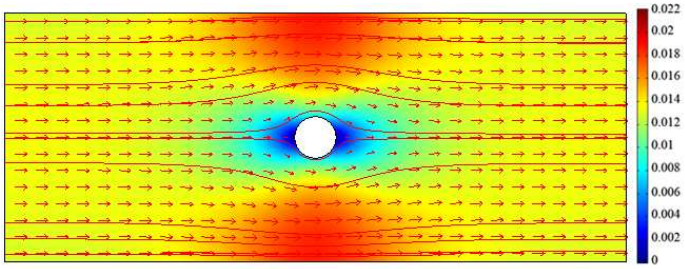

(d)

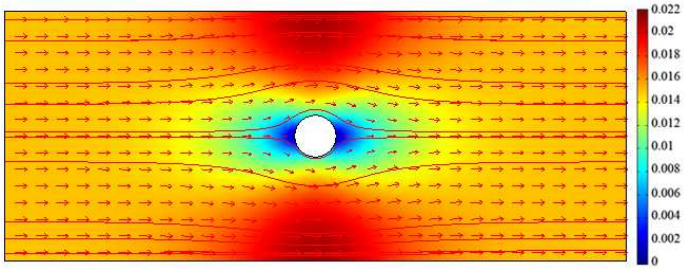

(e)

Figure 4.5: Streamlines and vector plots of the velocity fields in fluid in the micro channel for five different slip parameter values: (a) $l = 0$ (no slip), (b) $l = 0.25 \times 10^{-7}$, (c) $l = 0.5 \times 10^{-7}$, (d) $l = 1.0 \times 10^{-7}$, and (e) $l = 2.0 \times 10^{-7}$. The scaled bar shows the scale of the magnitude of velocity in m/s.

4.7 Movement of Particles

In the previous section, we study the flow behaviour of a Newtonian fluid passing around a spatially fixed particle in a microchannel and analyse the influence of slip boundary. In this section, we will focus on understanding the particle-fluid interaction and the particle flow driven by the fluid drag force. For this purpose, we consider the flow of a fluid with one, three, five and nine particles immersed in the fluid through a microchannel.

The computational domain is a horizontal channel with height of 6.2 $\mu\,\mathrm{m}$ and length of 45 $\mu\,\mathrm{m}$. The particles are circular with diameter of 0.5 $\mu\,\mathrm{m}$. The fluid is assumed to flow into the channel with speed $0.7\,\mathrm{mm/s}$ from the left to the right. The fluid properties are typical of human blood in capillary vessels with the viscosity η of $0.002\,\mathrm{Pa}\cdot\mathrm{s}$ and the density ρ_f of 1040 $\mathrm{kg/m^3}$. All particles are assumed to be solid particles with the material density of 1400 $\mathrm{kg/m^3}$.

The Arbitrary Lagrangian Eulerian approach as presented in section 4.3 is used to handle the dynamics of deforming geometry and the moving boundaries. New mesh coordinates on the channel area are calculated based on the movement of the particles. The Navier-Stokes equations are formulated in the moving coordinate system and are solved by the method presented in section 4.4.

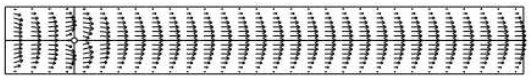

(a) $t = 0$ sec.

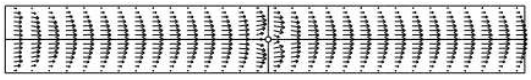

(b) $t = 1.62$ milli sec.

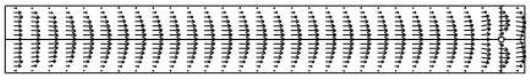

(c) $t = 2.43$ milli sec.

Figure 4.6: Velocity profiles at various instants of time for the case with one particle.

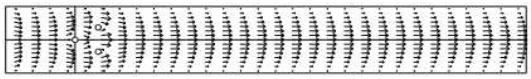

(a) $t = 0$ sec.

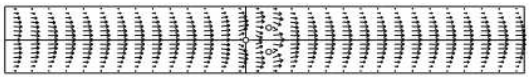

(b) $t = 0.81$ milli sec.

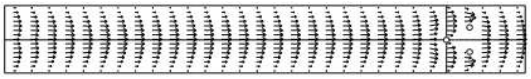

(c) $t = 1.18$ milli sec.

Figure 4.7: Velocity profiles at various instants of time for the case with three particles.

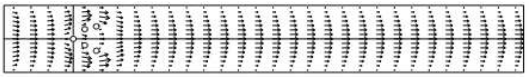

(a) $t = 0$ sec.

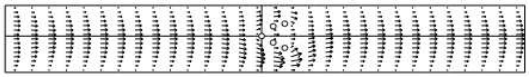

(b) $t = 0.69$ milli sec.

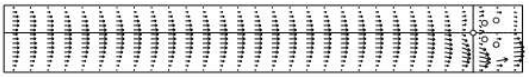

(c) $t = 1.02$ milli sec.

Figure 4.8: Velocity profiles at various instants of time for the case with five particles.

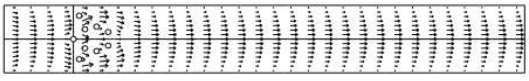

(a) $t = 0$ sec.

(b) $t = 0.39$ milli sec.

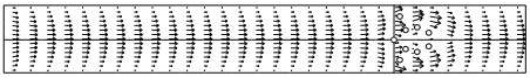

(c) $t = 0.53$ milli sec.

Figure 4.9: Velocity profiles at various instants of time for the case with nine particles.

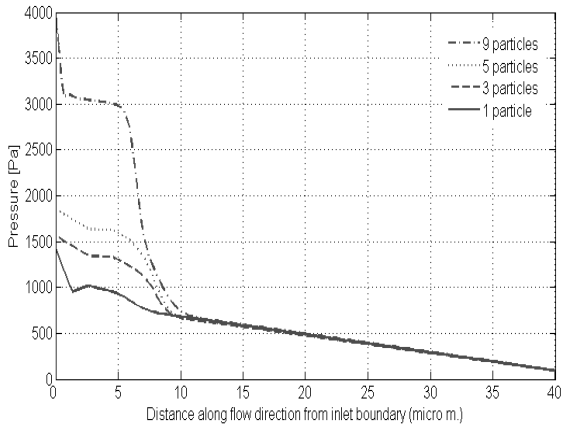

Figure 4.10: Pressure profiles along the flow direction at $t = 0s$.

Figures 4.6– 4.9 show the velocity profiles and particle positions at various instants of time for the cases with one, three, five and nine particles immersed in the fluid. Figure 4.10 shows the variation of the fluid pressure along the channel at a typical instants of time for the four cases. Obviously, except for the region near the particles, the velocity basically has the parabolic profile. It is also noted that the inlet pressure required to drive the flow increases significantly with the increase of the particle number. This is reasonable as larger pressure is required to drive the flow of more particles through the channel.

To understand the influence of the particle initial velocity $V_p(t_0)$, we consider three different cases of particle initial velocity, $V_p(t_0) = 0, V_p(t_0) = u(t_0)$, and $V_p(t_0) = 2u(t_0)$ where $V_p(t_0)$ is the particle initial velocity and $u(t_0)$ is the fluid velocity on the inlet of the channel.

Figures 4.11– 4.13 show the details of the evolution of the particle position, the forces acting on the particles as well as the particle velocity for the three cases of particle initial velocity.

For the case in which the particle initial velocity is zero, as shown in Figure 4.11, the drag force and consequently the total force acting on the particle is positive in the x-direction at the initial stage as the fluid velocity is larger than the particle velocity. This results in an acceleration of the particle and hence the particle velocity in the x-direction continues to increase and the particle move gradually to

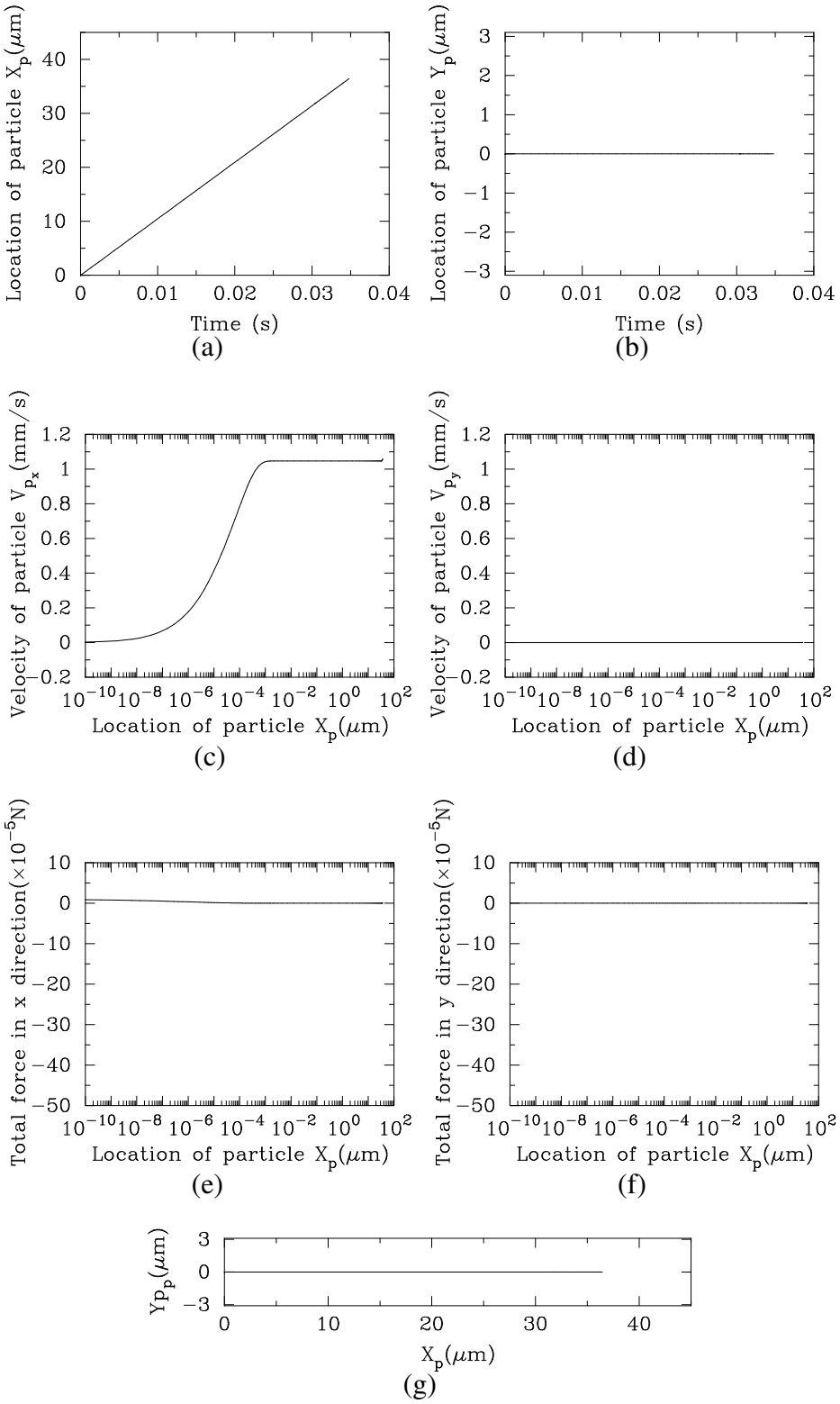

Figure 4.11: Computed results for the fluid-particle flow with $V_p(t_0) = 0$: (a)–(b) the x and y coordinates of the locations of the particle; (c)–(d) the x and y components of the particle velocity along the channel; (e)–(f) the x and y components of the total force acting on the particle; (g) the trajectory the of particle.

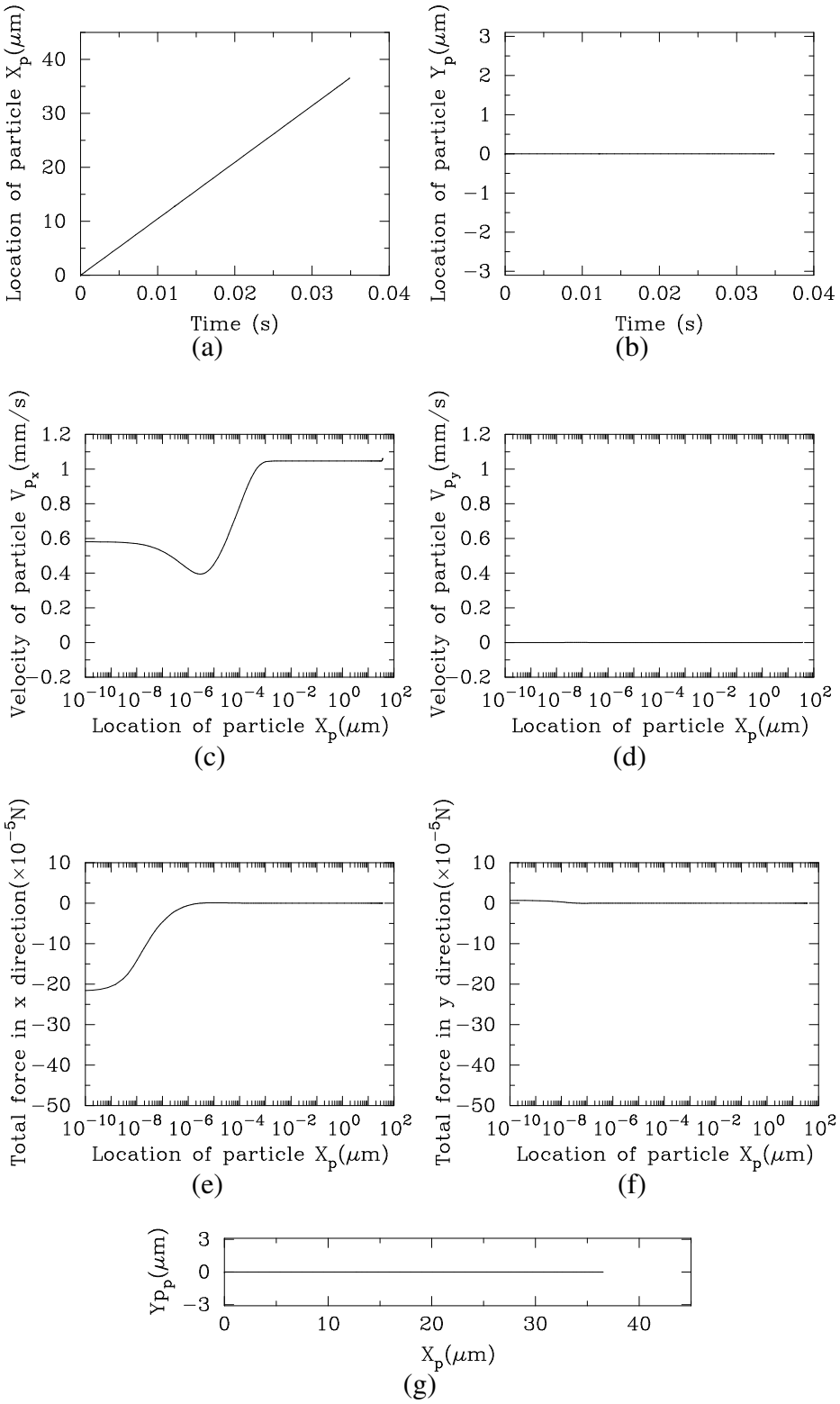

Figure 4.12: Computed results for the fluid-particle flow with $V_p(t_0) = u(t_0)$: (a)–(b) the x and y coordinates of the locations of the particle; (c)–(d) the x and y components of the particle velocity along the channel; (e)–(f) the x and y components of the total force acting on the particle; (g) the trajectory the of particle.

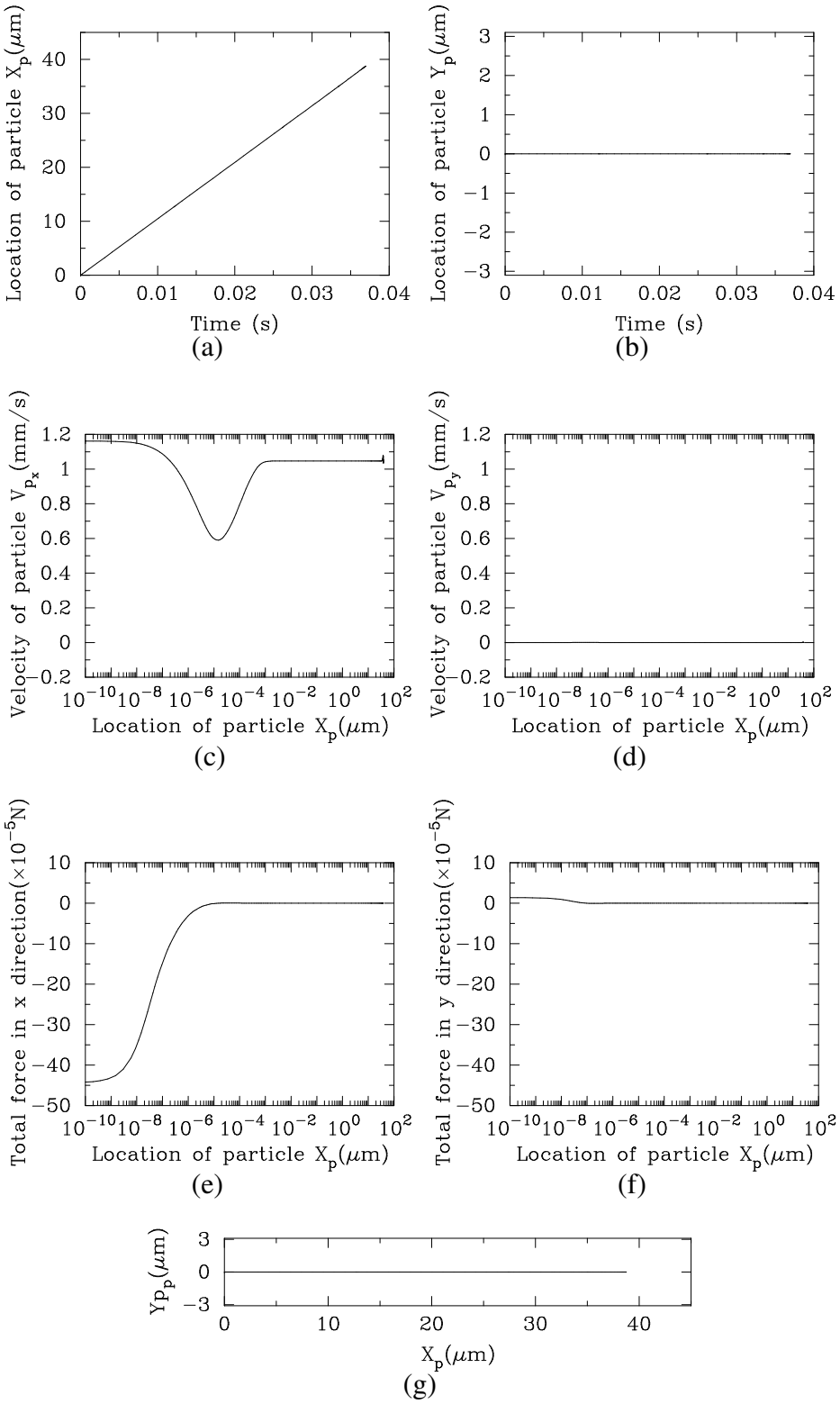

Figure 4.13: Computed results for the fluid-particle flow with $V_p(t_0) = 2u(t_0)$: (a)–(b) the x and y coordinates of the locations of the particle; (c)–(d) the x and y components of the particle velocity along the channel; (e)–(f) the x and y components of the total force acting on the particle; (g) the trajectory the of particle.

the right. When the particle velocity tends to the fluid velocity, the fluid drag force acting on the particle becomes zero and consequently the particle velocity remains constant as shown in figure 4.11 (e).

On the other extreme, when the particle moves much faster than the fluid, the fluid provides a resistance to the movement of the particle resulting in a negative total force acting on the particle in the x-direction. Consequently, the particle velocity decreases. Once the particle velocity decreases toward the fluid velocity, the total force acting on the particle tends to zero and consequently the particle velocity tends to a constant.

4.8 Concluding Remarks

A mathematical model and numerical technique for simulating particle-fluid flow in microchannels has been established. The model is then used to study the influence of boundary slip on the flow of a fluid through a microchannel, and to study the interaction force acting on the particles by the fluid and its resulting particle motion for various cases of particle initial velocity.

From the numerical results obtained, it can be concluded that the boundary slip between the fluid and the solid surface has very significant effect on the cross-section profile of the fluid velocity and the flow rate as well as the drag force acting on the immersed particles in the fluid.

It is also found that the inlet pressure required for driving the particles and fluid to flow with a required velocity increases very significantly with the increase of the number of particles immersed in the fluid. The results also indicate that the particle velocity will tend to constant after certain time after being injected into the fluid regardless its initial velocity.

Chapter 5

Movement of Particles in Fluids under Magnetic Forces

5.1 General Overview

To control magnetic particles (say drugs) to move in fluids to the target site, an external magnetic field is applied to generate a magnetic force acting on the particle [see 25]. The force is related to the magnetic field by the equation:

$$\mathbf{F}_{mag} = \frac{1}{\mu_r}(\mathbf{M} \cdot \nabla)\mathbf{B}, \tag{5.1}$$

where μ_r is the relative permeability of a magnetic material, $\mathbf{M} = (M_x, M_y, M_z)$ is the magnetization of the particle and $\mathbf{B} = (B_x, B_y, B_z)$ is the magnetic flux density.

In this chapter, we first present a mathematical model to describe the fluid-particle motion in fluids under magnetic forces. Then we apply the finite element method, based on the Arbitary Lagrangian-Eulerian approach, to solve the underlying boundary value problem. Finally we consider the control of particle movement in fluids.

The rest of the chapter is organized as follows. In section 5.2, the boundary value problem for the determination of the magnetic flux density are presented followed by the finite element method for the solution of the problem. In section 5.3, the equations for the particle motion in fluids under magnetic forces are presented. In section 5.4, a numerical investigation is undertaken on the control of particle movement in fluids under magnetic fields.

5.2 Modelling of Magnetic Fields

For static condition in stationary bodies, the magnetic flux density $\mathbf{B}$ is governed by Maxwell's equations:

$$\begin{aligned} \nabla \cdot \mathbf{B} &= 0, \\ \nabla \times \mathbf{H} &= \mathbf{0}, \end{aligned} \tag{5.2}$$

where the magnetic flux density $\mathbf{B}$ and the magnetic field strength $\mathbf{H}$ are related through the constitutive relation

$$\mathbf{B} = \mu_0 \mu_r \mathbf{H} + \mathbf{B}_r, \tag{5.3}$$

in which $\mathbf{B}_r = \mu_0 \mu_r \mathbf{M}$ denotes a residual flux density, μ_0 is the permeability in vacuum.

From the first equation of (5.2), the magnetic flux density can be determined from a vector potential by $\mathbf{B} = \nabla \times \mathbf{A}$ which identically satisfies the first equation of (5.2). Using the identity

$$\nabla \times (\nabla \times \mathbf{A}) = \nabla(\nabla \cdot \mathbf{A}) - \triangle \mathbf{A},$$

and the Coulomb gauge $\nabla \cdot \mathbf{A} = 0$, the second equation of (5.2) takes the form

$$\begin{aligned} &\nabla \times (\mu_0^{-1} \mu_r^{-1} \nabla \times \mathbf{A} - \mathbf{M}) = \mathbf{0}, \forall \mathbf{x} \in \Omega_{def} \\ &\text{or} \qquad \triangle \mathbf{A} = -\nabla \times (\mu_0 \mu_r \mathbf{M}), \end{aligned} \tag{5.4}$$

which is the vector-valued Poisson equation for the magnetic potential $\mathbf{A}$.

The boundary condition on particle surfaces is assumed to be insulation, that is,

$$\mathbf{n} \times \mathbf{A} = \mathbf{0}, \tag{5.5}$$

where $\mathbf{n}$ is the unit normal vector. Equations (5.4) and (5.5) form the boundary problem for the dertermination of the magnetic field.

For the convenience in formulation, we rewrite the governing equations for magnetic field in indicial notation as follows,

$$A_{i,jj} + \Big(\nabla \times (\mu_0 \mu_r \mathbf{M})\Big)_i = 0. \tag{5.6}$$

The field equations (5.6) are defined in $\Omega_{def}(t)$ with the boundary conditions (5.5). These equations and boundary conditions constitute a closed system of three partial differential equations in terms of three unknown functions A_1, A_2, and A_3. The system, supplemented by the boundary conditions (5.5) can be solved numerically to yield the magnetic vector potential $\mathbf{A}$.

The variational boundary value problem associated with the problem is as follows.

VBVP: Find $A_i \in \mathrm{H}^1(\Omega_{def})$ in the deformed mesh system at each time instant such that the Dirichlet boundary condition (5.5) is satisfied and for all $\hat{A}_i \in \mathrm{H}^1_{A_i}(\Omega_{def}) \equiv \{\hat{A}_i \in \mathrm{H}^1(\Omega_{def}) | \hat{A}_i = 0 \text{ on } \partial\Omega_{def_{A_i}}\}$

$$\left(A_{i,jj}, \hat{A}_i\right) + \left(\left(\nabla \times (\mu_0 \mu_r \mathbf{M})\right)_i, \hat{A}_i\right) = 0, \tag{5.7}$$

where $\mathrm{H}^1(\Omega_{def})$ is the Sobolev space $W^{1,2}(\Omega_{def})$ with norm $\| \cdot \|_{1,2,\Omega_{def}}$ and the inner product $(\cdot, \cdot)$ is defined by

$$(a, b) = \int_{\Omega_{def}} (ab) d\Omega. \tag{5.8}$$

Using integration by parts and the arbitary of $\hat{A}_i$, we have

$$\left(A_{i,j}, \hat{A}_{i,j}\right) - \left(\left(\nabla \times (\mu_0 \mu_r \mathbf{M})\right)_i, \hat{A}_i\right) = 0, \tag{5.9}$$

Since the computations are conducted in the reference coordinates, Ω, we need to transform equations (5.9) in the deformed coordinates to those equations in the reference coordinates. Through this, the inner product expression in (5.8) is re-defined as

$$(a, b) = \int_{\Omega_{def}} (ab) d\Omega = \int_{\Omega} (ab) \, |\mathbf{J}| \, d\Omega. \tag{5.10}$$

In the same way as that in chapter 4, the derivatives of the unknown functions A_i and the test functions $\hat{A}_i$ are determined by the following expressions:

$$\varphi_{i,j} = \varphi_{i,X_k} X_{k,j}, \tag{5.11}$$

$$\hat{\varphi}_{i,j} = \hat{\varphi}_{i,X_k} X_{k,j}. \tag{5.12}$$

Using (5.11) and (5.12), equations (5.13) become

$$\left(A_{i,j}, \hat{A}_{i,j}\right) - \left(\left(\nabla \times (\mu_0 \mu_r \mathbf{M})\right)_i, \hat{A}_i\right) = 0, \tag{5.13}$$

To find the solution of the above VBVP problem, the Bubnov-Galerkin finite element method is used. We choose an M-dimensional subspace $H_A^h \subset H_A^1(\Omega_{def})$ for A_i and the corresponding test function. Let $\{\phi_m^A\}_{m=1}^M$ be the basis functions of H^h which is an M-dimensional subspace of H^1. Then we have

$$A_i(\mathbf{X}, t) \approx (A_i)_h = \sum_{m=1}^{M} \phi_m^A(\mathbf{X})(A_i)_m(t), \tag{5.14}$$

$$\hat{A}_i(\mathbf{X}, t) \approx (\hat{A}_i)_h = \sum_{m=1}^{M} \phi_m^A(\mathbf{X})(\hat{A}_i)_m(t). \tag{5.15}$$

Substituting equations (5.14)–(5.15) into equations (5.13), and following the same procedure as in chapter 4, we can solve the boundary value problem for the magnetic vector potential $\mathbf{A}$ and consequently, the magnetic flux density.

5.3 Modelling of Particle Movement

The motion of particles in fluids under magnetic fields is governed by Newton's second law. As in chapter 4, we neglect the gravitational force, and hence the equations of motion for the particles in fluids under magnetic fields are as follows:

$$\begin{aligned} m_q \frac{\partial \mathbf{V}_q}{\partial t} &= \mathbf{F}_v + \mathbf{F}_q + \mathbf{F}_{\text{mag}}, \quad q = 1, 2, 3..., Q \\ \mathbf{V}_q|_{t=0} &= 0, \end{aligned} \tag{5.16}$$

where $\mathbf{F}_v$ is the fluid drag force acting on particle q by the fluid and can be determined by

$$\mathbf{F}_v = -\int_{\partial\Omega} \sigma \cdot \mathbf{n} dS,$$

in which σ is the stress in fluid and can be determined by the methods as presented in chapter 4. $\mathbf{F}_q$ are interaction forces acting on particle q by other particles and wall, namely

$$\mathbf{F}_q = \sum_{p=1, p\neq q}^{Q} \mathbf{F}_{q,p} + \sum_{w=1}^{2} \mathbf{F}_{q,w}, \tag{5.17}$$

in which

$$\mathbf{F}_{q,p} = \begin{cases} 0, \text{ for } d_{q,p} > R_q + R_p + \alpha \\ \frac{1}{\varepsilon_q}(\mathbf{X}_q - \mathbf{X}_p)(R_q + R_p + \alpha - d_{q,p})^2, \text{ for } d_{q,p} \leq R_q + R_p + \alpha \end{cases} \tag{5.18}$$

and

$$\mathbf{F}_{q,w} = \begin{cases} 0, \text{ for } d_{q,w} > 2R_q + \alpha \\ \frac{1}{\varepsilon_w}(\mathbf{X}_q - \mathbf{X}_w)(2R_q + \alpha - d_{q,w})^2, \text{ for } d_{q,w} \leq 2R_q + \alpha \end{cases} \tag{5.19}$$

where $d_{q,p}$ denotes the distance between the centers of the qth and pth particles, $d_{q,w}$ denotes the distance between the center of the qth particle and the imaginary particle on the other side of the wall, $\mathbf{X}_q$ and R_q are center and radius of the qth particle, α is the force range, and ε_q and ε_w are small positive stiffness parameters.

$\mathbf{F}_{\text{mag}}$ are magnetic forces acting on particle q which can be determined from (5.1). Also in a two dimension case, the magnetic potential is assumed to have a nonzero component only in the direction perpendicular to the plane, i.e., $\mathbf{A} = (0, 0, A_z)$. On $\partial\Omega_q$ and $\partial\Omega$, the magnetic potential is set to zero, that is, $A_z = 0$. The magnetization $\mathbf{M} = (M_x, M_y)$ for the magnetic source is given by $M_x = 0, M_y = 5 \times 10^4 A \cdot m^{-1}$, and for the magnetic particles

$$\begin{aligned} M_x &= a \arctan\left(\frac{b}{\mu_0\mu_r} A_{z,y}\right), \\ M_y &= a \arctan\left(-\frac{b}{\mu_0\mu_r} A_{z,x}\right), \end{aligned} \tag{5.20}$$

where a and b are two material parameters. Thus from (5.1), the magnetic force, $\mathbf{F}_{mag} = (F_{mag_x}, F_{mag_y})$, is given by

$$\begin{aligned} F_{mag_x} &= \frac{1}{\mu_r}(M_x A_{z,yx} + M_y A_{z,yy}), \\ F_{mag_y} &= \frac{1}{\mu_r}(-M_x A_{z,xx} - M_y A_{z,xy}). \end{aligned} \tag{5.21}$$

The position $\mathbf{X}_q$ of the center of the qth particle can be determined by the equation:

$$\begin{aligned} \frac{d\mathbf{X}_q}{dt} &= \mathbf{V}_q\,, \quad q = 1, 2, 3..., Q \\ \mathbf{X}_q|_{t=0} &= \mathbf{X}_q^0. \end{aligned} \tag{5.22}$$

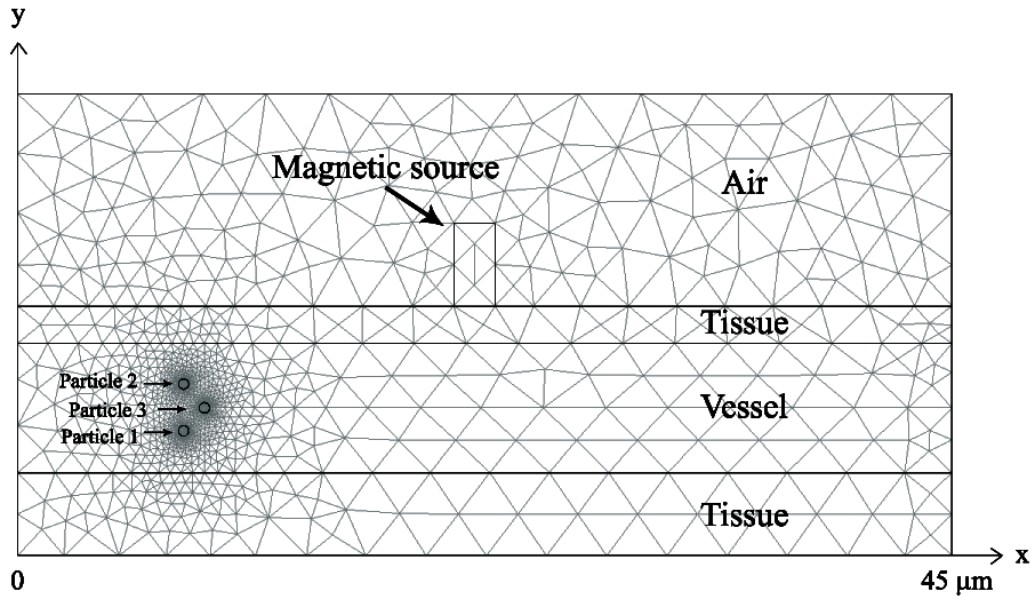

Figure 5.1: The computation domain, the location of magnetic source, and the finite element mesh.

5.4 A Numerical Study on the Control of Particle Movement

In this section, we numerically study the movement of particles in fluids in a small vessel with the surrounding materials as shown in Figure 5.1. The computation domain is a horizontal channel with height of $3.1\mu\,\mathrm{m}$ and length of $45\mu\,\mathrm{m}$. The particles are circular with diameter of $0.25\mu\,\mathrm{m}$. The fluid is assumed to flow into the channel with the speed of $0.7\,\mathrm{mm/s}$ from the left to the right. The fluid properties are typical of human blood with the viscostiy μ of $0.002\,\mathrm{Pa}\cdot\mathrm{s}$ and the density of $1040\,\mathrm{kg}\cdot\mathrm{m}^{-3}$. All particles are assumed to be solid particles with the same density of $1400\,\mathrm{kg}\cdot\mathrm{m}^{-3}$. The relative permeability μ_r is 5×10^3 for the magnet particles and 0.99998 for the tissue in the blood vessel. The material parameters a and b are $1\times10^{-4}\,\mathrm{A}\,/\,\mathrm{m}$ and $3\times10^{-5}(\mathrm{A}\,/\,\mathrm{m})^{-1}$, respectively.

Many cases with different number of magnetic particles are investigated and here we present the results for the case with one, three, five, and nine particles. Figure 5.1 shows the finite element mesh for the case with three particles. This typical mesh consist of 2956 elements.

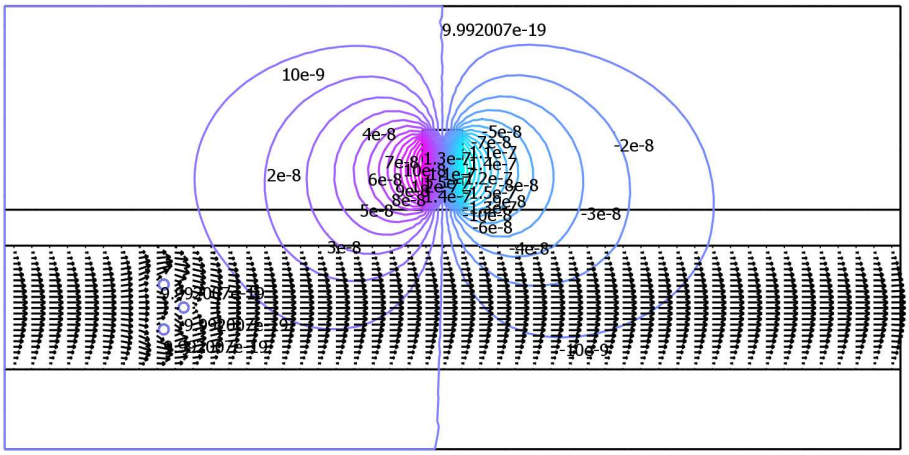

(a) $t = 0$ sec.

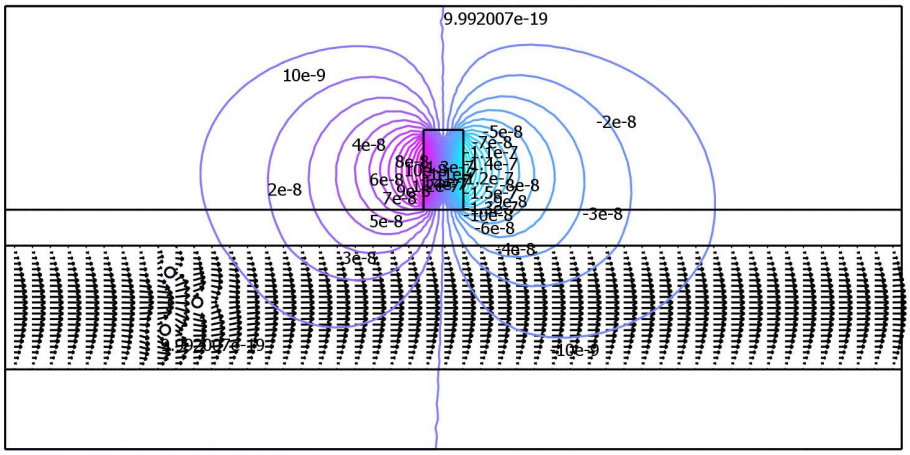

(b) $t = 0.01179$ sec.

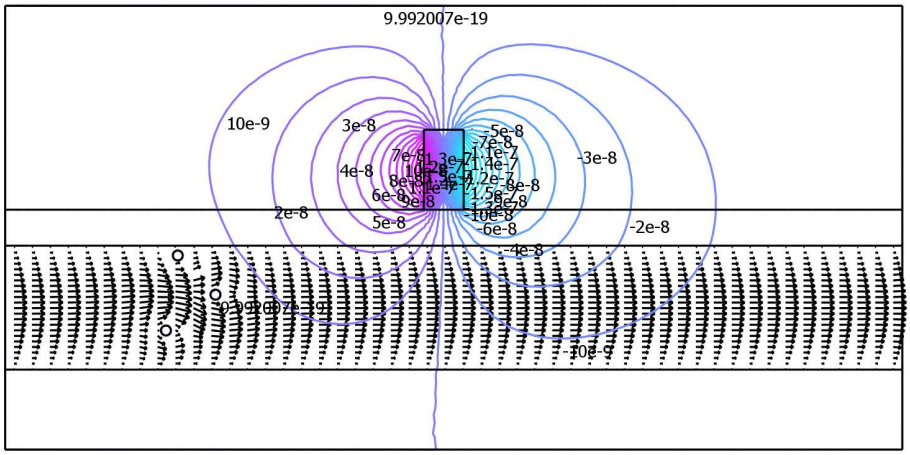

(c) $t = 0.017803$ sec.

Figure 5.2: Velocity profiles and particle locations at various instants of time for the case with three magnetic particles, shown together with the contour lines of the magnetic potential A_z.

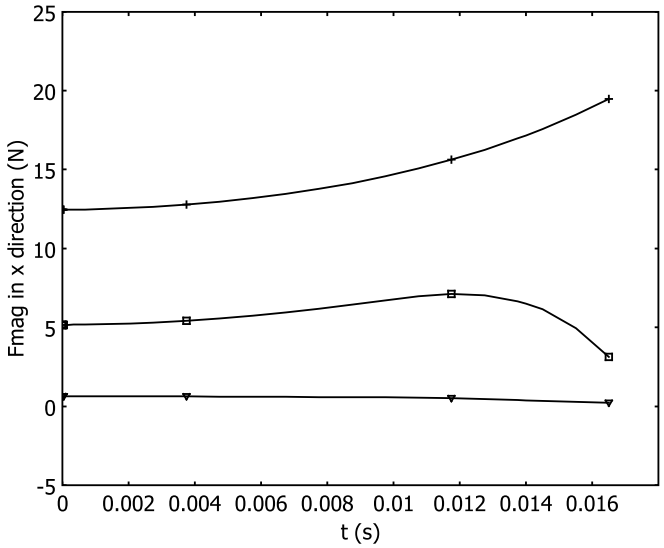

(a)

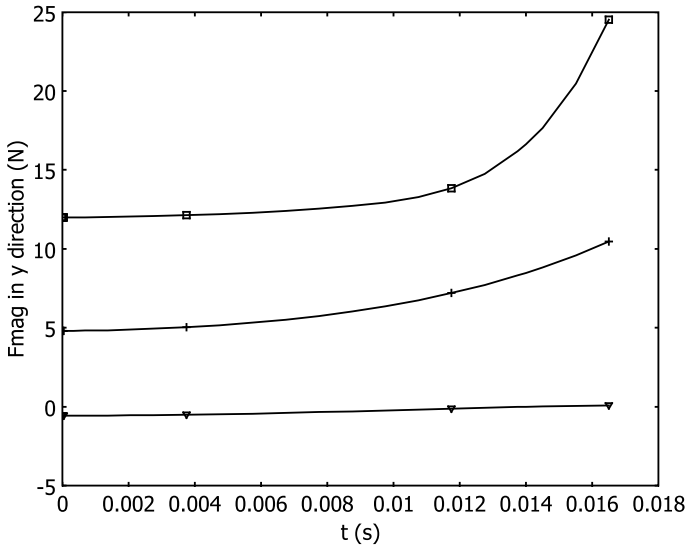

(b)

Figure 5.3: Magnetic forces acting on the particles for the three particles case: (a) the x-component of the magnetic force; and (b) the y-component of the magnetic force. The solid-triangle line is for particle 1; the solid-box line is for particle 2; and the solid-plus line is for particle 3.

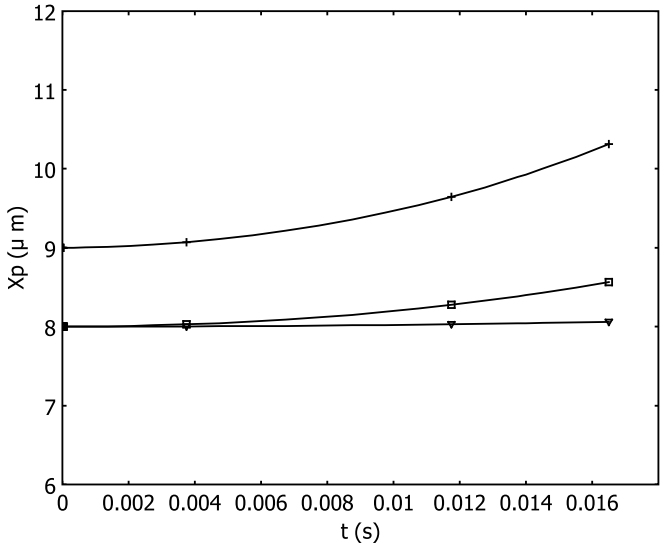

(a)

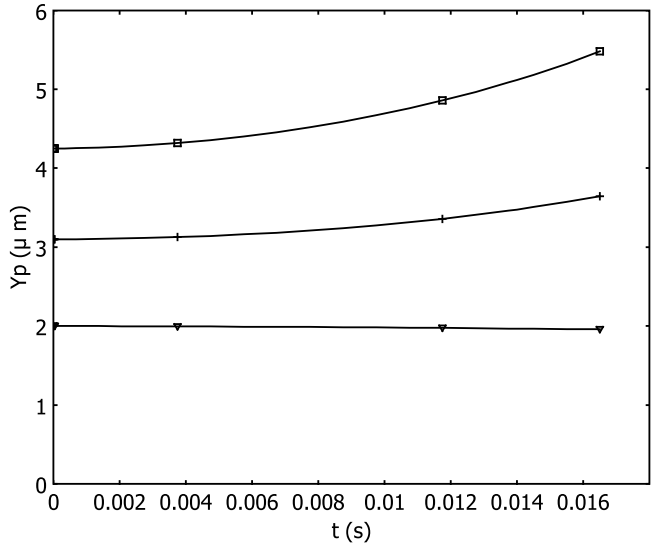

(b)

Figure 5.4: The location of the particles as a function of time for the three particles case: (a) the x-coordinate; (b) the y-coordinate. The solid-triangle line is for particle 1; the solid-box line is for particle 2; and the solid-plus line is for particle 3.

Figure 5.2 shows the velocity profiles and the particle locations at various instants of time for the case with three magnetic particles together with the contour lines of the magnetic potential A_z. Figure 5.3 shows the magnetic forces acting on the particles, while Figure 5.4 shows the locations of the particles as a function of time. The results show that the external magnetic source generates a magnetic field leading to magnetic forces acting on the magnetic particles. Under these magnetic forces and the fluid drag forces, the particle moves gradually toward the location of the magnetic source.

5.5 Concluding Remarks

A mathematical model has been constructed to simulate the fluid-particle flow under magnetic fields, and has been applied to study the blood flow and the magnetic particle flow in a capillary vessel with an external magnetic source. From the results, it can be concluded that the proposed model and technique are capable of simulating the particle flow in fluid under magnetic forces. The particles move toward the magnetic source. By changing the location of the magnetic source, one can control the particles to move to the desired target sites.

Chapter 6

Conclusions

6.1 Summary

This project focuses on the development of mathematical models, analytical and numerical methods for the study of three microflow problems including the transient flow of fluids through micro-annulus with boundary slip, the particle-fluid flow in microchannels, and the particle motion in fluids under magnetic forces. The results and conclusions gained from the research are summarized below under three aspects.

(1) A mathematical model has been developed to study the pressure gradient driving transient flow of fluid through micro-annulus with boundary slip and the exact solution for the problem has been derived. Based on the analytical expressions of the solutions, we analyse the influence of the slip parameter l and the geometry of the cross-section on the flow rate of fluid through the annual. The study shows that

(i) The influence of boundary slip on the flow through the annual is different for different types of pressure gradients. For flows driven by a constant pressure gradient, the flow rate always increases with the slip parameter l and achieves a linear increase rate for large l value; while, for the flows driven by the wave form pressure gradient with high frequency, the flow rate initially increases significantly as l increases from zero but tends to a constant when l becomes sufficiently large.

(ii) To achieve a fixed value of flow rate, one could have different (k, l) designs. The exact solutions obtained, together with the contour plots of the solutions, provide a tool for engineers and scientists to determine the proper (k, l) values.

(2) A mathematical model and numerical technique, based on the Arbitary Eulerian-Lagrangian approach and the finite element method, has been developed for simulating the particle-fluid flow in microchannels. Based on the model and the numerical technique, various investigations have been carried out and the investigations show that

(i) The boundary slip between the fluid and the solid surface has very significant effect on velocity profile of the fluid and the flow rate as well as the drag force acting on the immersed particles in the fluid. For $l = 0$ corresponding to the no-slip case, the velocity on the channel cross-section is basically parabolic except for the region close to the particles. As the slip parameter l increases, the velocity profile tends to uniform on the channel cross-section. Also, as l increased, the flow rate of fluid through the channel and the drag force acting on the immersed particles increase significantly.

(ii) The inlet pressure required for driving the particles and fluid to flow with a required velocity increases very significantly with the increase of the number of particles immersed in the fluid. Also, the particle velocity in fluid will tend to constant after certain time after being injected to the fluid regardless its initial velocity.

(3) A mathematical model and numerical technique has been established to study the motion of magnetic particles in fluid under magnetic fields generated by external magnetic sources. The model has been applied to study the blood flow and the movement of magnetic particles in the blood in a capillary vessel under an external magnetic source. The results show that the finite element based numerical technique is capable of simulating the particle flow in fluid under an external magnetic field. It is shown that the magnetic particles can

be controlled to move to the targeted site by changing the location of the external magnetic source.

6.2 Further Research

From the study, it can be concluded that mathematical modelling and numerical investigation can lead to a deeper understanding of the behaviour of fluid flow and particle flow in fluid in a micro-channel. Further work include: (a) study the fluid-particle flow in three dimension; (b) model blood flow at micro and/or nano scale based on non-Newtonian models.

Bibliography

[1] Noor Al Quddus, Walied A. Moussa and Subir Bhattacharjee. Motion of a spherical particle in a cylindrical channel using arbitrary lagrangian-eulerian method. *Journal of Colloid and Interface Science*, 317(2):620–630, 2008.

[2] Bassam Alfeeli, Daniel Cho, Mehdi Ashraf-Khorassani, Larry T. Taylor and Masoud Agah. Mems-based multi-inlet/outlet preconcentrator coated by inkjet printing of polymer adsorbents. *Sensors and Actuators B: Chemical*, 133(1):24 – 32, 2008.

[3] N. Ali and T. Hayat. Peristaltic motion of a carreau fluid in an asymmetric channel. *Applied Mathematics and Computation*, 193(2):535–552, 2007.

[4] J. Ally, B. Martin, M. B. Khamesee, W. Roa and A. Amirfazli. Magnetic targeting of aerosol particles for cancer therapy. *Journal of Magnetism and Magnetic Materials*, 293(1):442–449, 2005. 5th International Conference on Scientific and Clinical Applications of Magnetic Carriers MAY 20-22, 2004 Lyon, FRANCE.

[5] E. B. Arkilic, M. A. Schmidt and K. S. Breuer. Gaseous flow in long microchannels. *MicroElectroMechanical Systems*, 6(2):167–178, 1997.

[6] M. O. Aviles, A. D. Ebner and J. A. Ritter. Ferromagnetic seeding for the magnetic targeting of drugs and radiation in capillary beds. *Journal of Magnetism and Magnetic Materials*, 310(1):131–144, 2007.

[7] Misael O. Avils, Armin D. Ebner, Haitao Chen, Axel J. Rosengart, Michael D. Kaminski and James A. Ritter. Theoretical analysis of a transdermal ferro-

magnetic implant for retention of magnetic drug carrier particles. *Journal of Magnetism and Magnetic Materials*, 293(1):605–615, 2005.

[8] R. L. Batra and B. Jena. Flow of a casson fluid in a slightly curved tube. *International Journal of Engineering Science*, 29(10):1245–1258, 1991.

[9] J. Bikard, P. Menard, E. Peuvrel-Disdier and T. Budtova. 3d numerical simulation of the behaviour of a spherical particle suspended in a newtonian fluid and submitted to a simple shear. *Computational Materials Science*, 37(4):517–525, 2006.

[10] B. Bourlon, J. Wong, C. Miko, L. Forro and M. Bockrath. Nanoscale probe for fluidic and ionic transport. *Nature Nanotechnology*, 2(2):104–107, 2007.

[11] J. M. Buick. Lattice boltzmann simulation of power-law fluid flow in the mixing section of a single-screw extruder. *Chemical Engineering*, 64(1):52–58, 2009.

[12] H.M. Byrne and M.A.J. Chaplain. Mathematical models for tumour angiogenesis: numerical simulations and nonlinear wave solutions. *Bulletin of Mathematical Biology*, 57(3):461–486, 1995.

[13] C. Cai, Q. Sun and I. D. Boyd. Gas flows in microchannels and microtubes. *Journal of Fluid Mechanics*, 589:305–314, 2007.

[14] B.Y. Cao, M. Chen and Z.Y. Guo. Liquid flow in surface-nanostructured channels studied by molecular dynamics simulation. *Physical Review E*, 74(6, Part 2), 2006.

[15] B.Y. Cao, M. Chen and Z.Y. Guo. Velocity slip of liquid flow in nanochannels. *Acta Physica Sinica*, 55(10):5305–5310, 2006.

[16] G. Chauveteau. Rodlike polymer solution flow through fine pores: Influence of pore size on rheological behavior. *Journal of Rhelogy*, 26(2):111–142, 1982.

[17] H. T. Chen, D. Bockenfeld, D. Rempfer, M. D. Kaminski, X. Q. Liu and A. J. Rosengart. Preliminary 3-d analysis of a high gradient magnetic separator for biomedical applications. *Journal of Magnetism and Magnetic Materials*, 320:279–284, 2008.

[18] H. T. Chen, A. D. Ebner, M. D. Kaminski, A. J. Rosengart and J. A. Ritter. Analysis of magnetic drug carrier particle capture by a magnetizable intravascular stent-2: Parametric study with multi-wire two-dimensional model. *Journal of Magnetism and Magnetic Materials*, 293(1):616–632, 2005. 5th International Conference on Scientific and Clinical Applications of Magnetic Carriers MAY 20-22, 2004 Lyon, FRANCE.

[19] David Cheneler, Michael C.L. Ward, Michael J. Adams and Zhibing Zhang. Measurement of dynamic properties of small volumes of fluid using mems. *Sensors and Actuators B: Chemical*, 130(2):701 – 706, 2008.

[20] Beata Chertok, Allan E. David, Yongzhuo Huang and Victor C. Yang. Glioma selectivity of magnetically targeted nanoparticles: A role of abnormal tumor hydrodynamics. *Journal of Controlled Release*, 122(3):315–323, 2007.

[21] J. A. Cosgrove, J. M. Buick, S. J. Tonge, C. G. Munro, C. A. Greated and D. M. Campbell. Application of the lattice boltzmann method to transition of oscillatory channel flow. *Journal of Physics A: Mathematical and General*, 36(10):2609–2620, 2003.

[22] L. De Vargas and O. Manero. On the slip phenomenon of polymeric solutions through capillaries. *Polymer Engineering and Science*, 29(18):1232–1236, 1989.

[23] S. R. Deshmukh and D. G. Vlachos. Cfd simulations of coupled, countercurrent combustor/reformer microdevices for hydrogen production. *Industrial & Engineering Chemistry Research*, 44(14):4982–4992, 2005.

[24] C. F. Driscoll, R. M. Morris, A. E. Senyei, K. J. Widder and G. S. Heller. Magnetic targeting of microspheres in blood-flow. *Microvascular Research*, 27(3):353–369, 1984.

[25] A.H. Felix and M. Sylvain. Suggested shape for a first generation endovascular untethered microdevice prototype. In *Proceedings of the 2005 IEEE Engineering in Medicine and Biology 27th Annual Conference*, Shanghai, China, 1-4 September 2005.

[26] A.D. Fitt, A.R.H. Goodwin, K.A. Ronaldson and W.A. Wakeham. A fractional differential equation for a mems viscometer used in the oil industry. *Journal of Computational and Applied Mathematics*, In Press, Corrected Proof:–, 2008.

[27] E. J. Furlani and E. P. Furlani. A model for predicting magnetic targeting of multifunctional particles in the microvasculature. *Journal of Magnetism and Magnetic Materials*, 312(1):187–193, 2007.

[28] M. Gad-el Hak. The fluid mechanics of microdevices - the freeman scholar lecture. *Journal of Fluids Engineering*, 121(1):5–33, 1999.

[29] W. Gao and J. Wang. Similarity solutions to the power-law generalized newtonian fluid. *Journal of Computational and Applied Mathematics*, 222(2):381–391, 2008.

[30] S. Goodwin, C. Peterson, C. Hoh and C. Bittner. Targeting and retention of magnetic targeted carriers (mtcs) enhancing intra-arterial chemotherapy. *Journal Of Magnetism And Magnetic Materials*, 194(1-3):132–139, 1999.

[31] John Greenman, Antonia Galvez, Lorenzino Giusti and Ioannis Ieropoulos. Electricity from landfill leachate using microbial fuel cells: Comparison with a biological aerated filter. *Enzyme and Microbial Technology*, 44(2):112 – 119, 2009.

[32] A. D. Grief and G. Richardson. Mathematical modelling of magnetically

targeted drug delivery. *Journal Of Magnetism And Magnetic Materials*, 293(1):455–463, 2005.

[33] H. Herwig and O. Hausner. Critical view on new results in micro-fluid mechanics: An example. *International Journal of Heat and Mass Transfer*, 46(5):935–937, 2003.

[34] V. Hessel, C. Knobloch and H. Lowe. Review on patents in microreactor and micro process engineering. *Recent Patents on Chemical Engineering*, 1:1–16, 2008.

[35] C. M. Ho and Y. C. Tai. Micro-electro-mechanical systems (mems) and fluid flows. *Annual Review of Fluid Mechanics*, 30:579–612, 1998.

[36] H. H. Hu. Direct simulation of flows of solid-liquid mixtures. *International Journal of Multiphase Flow*, 22(2):335 – 352, 1996.

[37] P. Huang and K. S. Breuer. Direct measurement of slip length in electrolyte solutions. *Physics of Fluids*, 19(2):028104–+, February 2007.

[38] P. Huang and K. S. Breuer. Direct measurement of slip length in electrolyte solutions. *Physics of Fluids*, 19:028104, 2007.

[39] Yeny Hudiono, Sunho Choi, Shu Shu, William J. Koros, Michael Tsapatsis and Sankar Nair. Porous layered oxide/nafion? nanocomposite membranes for direct methanol fuel cell applications. *Microporous and Mesoporous Materials*, 118(1-3):427 – 434, 2009.

[40] S. C. Hunter. *Mechanics of Continuous Media*. New York: John Wiley & Sons, 1983.

[41] Z. Ismail, I. Abdullah, N. Mustapha and N. Amin. A power-law model of blood flow through a tapered overlapping stenosed artery. *Applied Mathematics and Computation*, 195(2):669–680, 2008.

[42] Barbara M. Johnston, Peter R. Johnston, Stuart Corney and David Kilpatrick. Non-newtonian blood flow in human right coronary arteries: steady state simulations,. *Journal of Biomechanics*, 37(5):709 – 720, 2004.

[43] Puneet Khanna, Alejandro Villagra, Sangchae Kim, Edward Seto, Mark Jaroszeski, Ashok Kumar and Shekhar Bhansali. Use of nanocrystalline diamond for microfluidic lab-on-a-chip. *Diamond and Related Materials*, 15(11-12):2073 – 2077, 2006. Proceedings of the joint 11th International Conference on New Diamond Science and Technology and the 9th Applied Diamond Conference 2006 - ICNDST-ADC 2006.

[44] A. J. C. Ladd. Numerical simulations of particulate suspensions via a discretized boltzmann equation. i. theoretical foundation. *Journal of Fluid Mechananics*, 271:285–309, 1994.

[45] E. Lauga and T. M. Squires. Brownian motion near a partial slip boundary: A local probe of the no-slip condition. *Physics of Fluids*, 17:103102, 2005.

[46] H. B. Lee, I. W. Yeo and K. K. Lee. Water flow and slip on napl-wetted surfaces of a parallel-walled fracture - art. no. l19401. *Geophysical Research Letters*, 34(19):19401, 2007.

[47] Howard A. Levine, Serdal Pamuk, Brian D. Sleeman and Marit Nilsen-Hamilton. Mathematical modeling of capillary formation and development in tumor angiogenesis: Penetration into the stroma. *Bulletin of Mathematical Biology*, 63(5):801–863, September 2001.

[48] B. M. Li and D. Y. Kwok. A lattice boltzmann model for electrokinetic microchannel flow of electrolyte solution in the presence of external forces with the poisson-boltzmann equation. *International Journal of Heat and Mass Transfer*, 46(22):4235–4244, 2003.

[49] Bingcheng Lin and Jianhua Qin. Lab on a chip: A key platform for medical diagnostics and drug screening. *Journal of Biotechnology*, 136(Supplement

1):S172 – S172, 2008. Biotechnology for the Sustainability of Human Society - IBS 2008 Abstracts, 13th International Biotechnology Symposium and Exhibition.

[50] P. W. Longest, C. Kleinstreuer and J. R. Buchanan. Efficient computation of micro-particle dynamics including wall effects. *Computers & Fluids*, 33(4):577–601, 2004.

[51] V. C. Loukopoulos and E. E. Tzirtzilakis. Biomagnetic channel flow in spatially varying magnetic field. *International Journal Of Engineering Science*, 42(5-6):571–590, 2004.

[52] A. Mandal, M. A. Jog and A. A. Ibrahim. Flow of power-law fluids in simplex atomizers. *International Journal of Heat and Fluid Flow*, 29(5):1494–1503, 2008.

[53] N. Mangadoddy, R. Prakash, R. P. Chhabra and V. Eswaren. Forced convection in cross flow of power law fluids over a tube bank. *Chemical Engineering*, 59(11):2213–2222, 2004.

[54] M. J. Martin and I. D. Boyd. Momentum and heat transfer in a laminar boundary layer with slip flow. *AIAA Journal of Thermophysics and Heat Transfer*, 20(4):710–719, 2006.

[55] M. T. Matthews and J. M. Hill. Newtonian flow with nonlinear navier boundary condition. *Acta Mechanica*, 191(3-4):195–217, 2007.

[56] M. Mooney and S. A. Black. A generalized fluidity power law and laws of extrusion. *Journal of Colloid Science*, 7(3):204–217, 1952.

[57] K. Mosbach and U. Schroder. Preparation and application of magnetic polymers for targeting of drugs. *Febs Letters*, 102(1):112–116, 1979.

[58] J. J. Nakane, M. Akeson and A. Marziali. Nanopores sensors for nucleic acid analysis. *Journal of Physics Condensed Matter*, 15:R1365, 2005.

[59] C. M. Oldenburg, S. E. Borglin and G. J. Moridis. Numerical simulation of ferrofluid flow for subsurface environmental engineering applications. *Transport In Porous Media*, 38(3):319–344, 2000.

[60] Q. A. Pankhurst, J. Connolly, S. K. Jones and J. Dobson. Applications of magnetic nanoparticles in biomedicine. *Journal Of Physics D-Applied Physics*, 36(13):R167–R181, 2003.

[61] J. P. Pascal. Instability of power-law fluid flow down a porous incline. *Journal of Non-Newtonian Fluid Mechanics*, 133(2-3):109–120, 2006.

[62] R. G. Pereira. Additional effects on internal flow of non-newtonian fluids in the presence of a particle. *Journal of Non-Newtonian Fluid Mechanics*, 95(2-3):85–100, 2000.

[63] R. Pit, H. Hervet and L. Leger. Direct experimental evidence of slip in hexadecane: Solid interfaces. *Physical Review Letters*, 85(5):980–983, 2000.

[64] W. Risau. *Nature*, chapter Mechanisms of angiogenesis, pages 671–674. Number 386. 1997.

[65] O. Rotariu and N. J. C. Strachan. Modelling magnetic carrier particle targeting in the tumor microvasculature for cancer treatment. *Journal of Magnetism and Magnetic Materials*, 293(1):639–646, 2005. 5th International Conference on Scientific and Clinical Applications of Magnetic Carriers MAY 20-22, 2004 Lyon, FRANCE.

[66] E. K. Ruuge and A. N. Rusetski. Magnetic fluids as drug carriers: Targeted transport of drugs by a magnetic field. *Journal of Magnetism and Magnetic Materials*, 122(1-3):335–339, April 1993.

[67] K. C. Sahu, P. Valluri, P. D. M. Spelt and O. K. Matar. Linear instability of pressure-driven channel flow of a newtonian and a herschelbulkley fluid. *Physics of Fluids*, 19(12):122101, 2007.

[68] F. Saidi. Non-newtonian flow in a thin film with boundary conditions of coulombs type. *Zamm-Zeitschrift Fur Angewandte Mathematik Und Mechanik*, 86(9):702–721, 2006.

[69] Hirofumi Shintaku, Shosaku Imamura and Satoyuki Kawano. Microbubble formations in mems-fabricated rectangular channels: A high-speed observation. *Experimental Thermal and Fluid Science*, 32(5):1132 – 1140, 2008.

[70] P. Singh, D. D. Joseph, T. I. Hesla, R. Glowinski and T. W. Pan. A distributed lagrange multiplier/fictitious domain method for viscoelastic particulate flows. *Journal Of Non-Newtonian Fluid Mechanics*, 91(2-3):165–188, 2000.

[71] J. C. Slattery. *Advanced Transport Phenomena*. New York: Cambridge University Press, 1999.

[72] Kristian Smistrup, Peter T. Tang, Ole Hansen and Mikkel F. Hansen. Microelectromagnet for magnetic manipulation in lab-on-a-chip systems. *Journal of Magnetism and Magnetic Materials*, 300(2):418 – 426, 2006.

[73] C. W. Soh and E. W. Mureithi. Exact and numerical solutions of a fully developed generalized second-grade incompressible fluid with power-law temperature-dependent viscosity. *International Journal of Non-Linear Mechanics*, 41(2):271–280, 2006.

[74] J. Stohr and H. C. Siegmann. *Magnetism*. New York; Springer-Verlag, 2006.

[75] A. Stphanou, S.R. McDougall, A.R.A. Anderson and M.A.J. Chaplain. Mathematical modelling of flow in 2d and 3d vascular networks: Applications to anti-angiogenic and chemotherapeutic drug strategies. *Mathematical and Computer Modelling*, 41(10):1137–1156, May 2005.

[76] Y. C. Su and L. W. Lin. A water-powered micro drug delivery system. *Journal of Microelectromechanical Systems*, 13(1):75–82, 2004.

[77] L. Szalmas. Slip-flow boundary condition for straight walls in the lattice boltzmann model - art. no. 066710. *Physical Review*, E7306(6):6710, 2006.

[78] Nomura Takashi and Thomas J.R. Hughes. An arbitrary lagrangian-eulerian finite element method for interaction of fluid and a rigid body. *Computer Methods in Applied Mechanics and Engineering*, 95(1):115 – 138, 1992.

[79] P. A. Thompson and S. M. Troian. A general boundary condition for liquid flow at solid surfaces. *Nature*, 389:360–362, 1997.

[80] A. Tosi, L. Capretto, C. Anselmi and C. Nastruzzi. Lipid based microparticles for lab-on-a-chip application: Factorial design evaluation of influence of formulation and process parameters. *Journal of Controlled Release*, 132(3):e56 – e58, 2008. Proceedings of the Tenth European Symposium on Controlled Drug Delivery.

[81] M. J. Tretheway and C. D. Meinhart. Apparent fluid slip at hydrophobic microchannel walls. *Physics of Fluids*, 14(3):L9–L12, 2002.

[82] R. Tuinier and T. Taniguchi. Polymer depletion-induced slip near an interface. *Journal of Physics Condensed Matter*, 17:L9–L14, 2005.

[83] E. E. Tzirtzilakis, M. Xenos, V. C. Loukopoulos and N. G. Kafoussias. Turbulent biomagnetic fluid flow in a rectangular channel under the action of a localized magnetic field. *International Journal of Engineering Science*, 44(18-19):1205–1224, 2006.

[84] P. A. Voltairas, D. I. Fotiadis and L. K. Michalis. Hydrodynamics of magnetic drug targeting. *Journal of Biomechanics*, 35(6):813–821, 2002.

[85] K. Watanabe and H. Yanuar, Mizunuma. Slip of newtonian fluids at solid boundary. *JSME International Journal Series B*, 41(3):525–529, 1998.

[86] K. J. Widder, R. M. Morris, G. Poore, D. P. Howard and A. E. Senyei. Tumor remission in yoshida sarcoma-bearing rats by selective targeting of magnetic

albumin microspheres containing doxorubicin. *Proceedings Of The National Academy Of Sciences Of The United States Of America-Biological Sciences*, 78(1):579–581, 1981.

[87] B. Wiwatanapataphee, D. Poltem, Y. H. Wu and Y. Lenbury. Simulation of pulsatile flow of blood in stenosed coronary artery bypass with graft. *Mathematical Biosciences and Engineering*, 3(2):371–383, 2006.

[88] B. Wiwatanapataphee, Y. H. Wu, J. Archapitak, P. F. Siew and B. Unyong. A numerical study of the turbulent flow of molten steel in a domain with a phase-change boundary. *Journal of Computational and Applied Mathematics*, 166(1):307–319, 2004.

[89] Y. H. Wu and B. Wiwatanapataphee. Modelling of turbulent low and multiphase heat transfer under electromagnetic force. *Discrete and Continuous Dynamical Systems-Series B*, 8(3):695–706, 2007.

[90] Y. H. Wu, B. Wiwatanapataphee and M. Hu. Pressure-driven transient flows of newtonian fluids through microtubes with slip boundary. *Physica A: Statistical Mechanics and its Applications*, 387(24):5979–5990, 2008.

[91] J. L. Xu and Y. X. Li. Boundary conditions at the solid-liquid surface over the multiscale channel size from nanometer to micron. *International Journal of Heat and Mass Transfer*, 50(13-14):25712581, 2007.

[92] S. P. Yang and K. Q. Zhu. Analytical solutions for squeeze flow of bingham fluid with navier slip condition. *Journal of Non-Newtonian Fluid Mechanics*, 138(2-3):173–180, 2006.

[93] C. Ybert, C. Barenti, C. Cottin-Bizonne, P. Joseph and L. Bocquet. Achieving large slip with superhydrophobic surfaces: Scaling laws for generic geometries. *Physics of Fluids*, 19:123601, 2007.

[94] H. A. Yousif and R. Melka. Bessel function of the first kind with complex argument. *Computer Physics Communications*, 106(3):199–206, 1997.

[95] Y. X. Zhu and S. Granick. Rate-dependent slip of newtonian liquid at smooth surfaces - art. no. 096105. *Physical Review Letters*, 8709(9):6105, 2001.

[96] O.C. Zienkiewicz, R.L. Taylor and P. Nithiarasu. *Finite Element Method for Fluid Dynamics (6th Edition)*. Elsevier, 2005.